UC Berkeley

UC Berkeley Previously Published Works

Title

CHAPTER 8 Aromatic Molecules on Metallic Surfaces: Structure and Reactivity

Permalink

ISBN

Authors

Marangoni, Tomas
Cloke, Ryan R
Fischer, Felix R

Publication Date

2016

DOI

Peer reviewed

CHAPTER X

Aromatic Molecules On Metallic Surfaces: Structure And Reactivity

Dr. Tomas Marangoni[1], Dr. Ryan R. Cloke[1], Prof. Felix R. Fischer[1,2,3]*

[1]Department of Chemistry, University of California Berkeley, Berkeley, California 94720, United States

[2]Materials Sciences Division, Lawrence Berkeley National Laboratory, Berkeley, California 94720, United States

[3]Kavli Energy NanoSciences Institute at the University of California Berkeley and the Lawrence Berkeley National Laboratory, Berkeley, California 94720, United States

*Corresponding contributor. E-mail: ffischer@berkeley.edu

Abstract

In this chapter, a decade-long series of investigations about aromatic molecules on metallic surfaces has been reviewed. The most relevant studies regarding both structural investigation and chemical reactivity of aromatic systems on metallic surface is described. A major emphasis has been placed on the investigation techniques that allow for a direct visualization of the structural and electronic properties of both isolated and extended aromatic systems on surface (*e.g.* Scanning Tunnelling Microscopy, non contact-Atomic Force Microscopy and Kelvin Probe Force Microscopy). The synthesis, imaging and characterization of structure such as extended polyaromatic hydrocarbon, 1-D assembly, 2-D network and Graphene Nanoribbons are discussed. Among the different types of reactions, surface mediated reactions, such as acetylene homocoupling, cyclodehydrogenation, cycloaddition and metal-coordination, have been described.

Table of Contents

X.**1 Introduction**

The deposition of molecules featuring an extended conjugated system in thin-films, self-assembled monolayers (SAMs) or as molecularly isolated species, on solid supports has emerged as a valuable tool to rationally engineer functional architecture with novel and unprecedented electronic properties.[1-8] Despite the wide variety of techniques nowadays available to deposit molecules on a surface[9-12] (vapor deposition, spin and drop-casting, *Langmuir-Blodgett* films, etc.), the investigation of the intra- and intermolecular interaction of molecules deposited on inorganic surfaces remains a very challenging task. In this context, the study of interactions between aromatic molecules in thin films and on surfaces covers a broad field of applications. Given the multitude of possible interactions and the broad range of associated energies the underlying self-assembly processes are largely treated phenomenologically (*e.g.* 2-D spatial constrain and surface-molecule interactions).

Due to the broad scientific scope and the complexity of self-assembly processes on surfaces, we herein do not attempt to provide an exhaustive review of the literature. We will instead focus our attention on the most important studies investigating the structural characteristics and the reactivity of extended aromatic systems deposited on metal surfaces.

In the last decades, extensive experimental and theoretical efforts have been dedicated to elucidate the interactions of organic molecules with inorganic crystalline solids.[13-17] The interface between organic and inorganic phases in hybrid materials has shown to be responsible for key functions in many types of electronic devices ranging from Organic Light Emitting Diodes (OLED) and Organic Thin Film Transistors (OTFT) to Organic Photovoltaics (OPV).[18-24] The key advantages for using organic functional materials as components in electronic devices lie in their light-weight, high mechanical flexibility and ease of industrial processing.

The nature and properties of the interface between aromatic organic semiconductors and their inorganic substrates have been shown to play a significant role in the performance of the device, influencing parameters such as the local density of states at the interface or the contact resistance. One of the most crucial factors, which dictate the properties of such interfaces, is the nature of the bond formed between the molecules and the substrate. The two main types of interactions that can occur during the adsorption process at the organic-inorganic interface are chemical (*i.e.* chemisorption) or physical (*i.e.* physisorption) adsorption. The former is generally defined as an adsorption process in which the forces that bind the molecule to the substrate are strong chemical interactions (*e.g.* covalent, ionic, or strong polar bonding), whereas the latter refers to the adsorption of molecules through relatively nonspecific Van der Waals or dispersion interactions.[25] Due to the lack of strong interactions with the surface, the physisorbed molecule will largely conserve its structural integrity and orbital structure upon surface adsorption. On the other hand

during chemisorption, the orbital structure of the adsorbed molecule will be altered by the hybridization with the electronic wavefunction of the surface states.

As a first approximation, this simple model describes the absorption process of small molecules. The behaviour and the properties of extended π-conjugated systems on metallic surfaces instead are much less understood. Therefore the precise characterization of the structures and electronic properties of organic aromatic molecules adsorbed on metal surface is critical to understand this fundamental interaction. Initially, this chapter will focus on the most significant developments in the characterization of π-conjugated molecular systems on metallic surfaces, with a particular emphasis on their direct structural elucidation. In the second part, the focus will be instead shifted to the reactivity of aromatic molecular units on surfaces leading to the rational assembly of complex architecture such as covalent 2D-networks, 1-D polymers and Graphene Nanoribbons (GNR).

X.2 Structural Investigations of Aromatic Molecules on Surfaces

X.2.1 General Surface Characterization Techniques

Morphological characterization of a substrate can be achieved using microscopic techniques such as Transmission Electron Microscopy (TEM) and Scanning Electron Microscopy (SEM), which enable the acquisition of images with a resolution several orders of magnitude greater than conventional optical microscopy. Furthermore, the constant development of Scanning Probe Microscopy (SPM), such as Scanning Tunnelling Microscopy (STM) or Atomic Force Microscopy (AFM), has provided the possibility to directly visualize the structure of surface immobilized molecules and nanostructures with molecular and sometimes even sub-molecular resolution (*vide infra*). The elemental composition and chemical state of material surface are among the most useful and basic information and can be obtained by X-ray Photoelectron Spectroscopy (XPS) or Energy Dispersive X-ray spectroscopy (EDX). Both techniques exploit the interaction of high energy X-ray radiation with a sample surface in order to obtain information about the elemental composition. In particular, XPS spectra can be obtained by exciting the sample with an X-ray source in a high vacuum (or ultra-high vacuum) chamber and measuring the kinetic energy of the electrons that are emitted from a narrow layer (0–10 nm depth) close to the surface of the material. Through XPS, it is possible to obtain important information about the analysed materials, such as elemental composition of the material surface (with part per thousand sensitivity), its empirical formula, the chemical and electronic states of atoms at the surface and the uniformity of the elemental composition.

Another important structural characterization technique is Raman spectroscopy. Excitation with a monochromatic laser can be used to probe characteristic vibrational modes of a molecule adsorbed on a surface. Since these excitations are strictly related to the chemical symmetry and type of bonds present in

the material, Raman spectroscopy has been used as an alternative structural characterization method that provides fingerprint spectra by which molecules and materials can be identified. Additionally, having the advantage of being a pure diffractive technique, Raman spectroscopy can also be coupled to optical microscopy to create confocal Raman microscopy that merges the possibility to perform high magnification visualisation of a sample and *in situ* Raman analysis.

X.2.2 Visualization Techniques with Submolecular Resolution: STHM and nc-AFM

With the recent expansion of Scanning Probe Microscopy (SPM), adsorption of organic molecules on inorganic conductive surfaces (*i.e.* metallic) has become one of the most valuable approaches to investigate their structural, chemical and physical properties. Scanning Tunnelling Microscopy, an imaging technique invented by *Gerd Binning* and coworkers in 1981, was the first type of SPM technique developed that was able to image inorganic conductive surfaces with atomic resolution.[26] In its classical design, a Scanning Tunnelling Microscope (STM) is composed of an atomically sharp metallic probe (generally made of tungsten or a platinum-iridium alloy), which is scanned along the xy plane of a conductive surface at a distances of few Å, while applying a voltage between the surface and the probe (Figure X.1).[27, 28] The application of a voltage between two conducting materials, separated by a small insulating gap (typically 0.3-1.0 nm), leads to a tunnelling current between the probe and the surface. Since the intensity of the tunnelling current depends on the tip-sample distance, the applied voltage V and the tip/sample local density of states (LDOS), even the slightest variation of the sample surface can be detected using this method.
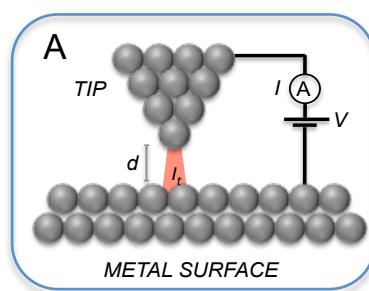

Figure X.1 Schematic representation (A) of a Scanning Tunneling Microscope. Tunnelling current between the tip and the metal surface depicted in red (*d*: distance between tip and sample, I_t: tunnelling current).[28]

From the experimental point of view, on-surface investigations can generally be performed using two different STM modes. In the first and most intuitive mode, named *constant height* mode, the tip is held at a fixed z-position while scanning across the sample surface at a constant bias voltage. In this setting, the variation in the tunnelling current induced by changes in the tip-sample distance is recorded as a function of the tip position and can be used to reconstruct a topographic image of the surface. In the second mode, called *constant current* mode, the distance between tip and sample is continuously adjusted electronically by

a feedback loop in order to maintain a constant user-defined tunnelling current. The final STM image is then reconstructed from the feedback signal.

From the time of its invention, Scanning Tunnelling Microscopy has been used to investigate the structure and properties of a wide range of molecules and materials such as isolated organic and bio-molecules, supramolecular systems and 2-D inorganic crystals. [29-33] However, although atomic resolution has been obtained for a wide range of crystalline surfaces, atomic resolution on molecules adsorbed on metallic surface has only been achieved very recently. Two SPM techniques able to achieve such kind of spatial resolution are Scanning Tunnelling Hydrogen Microscopy (STHM) and Non-Contact Atomic Force Microscopy (nc-AFM). [33] In both cases, the key to enable the direct visualization of individual bonds and atoms in individual molecules is the functionalization of the probe with diatomic molecules, such as dihydrogen or carbon monoxide for STHM and nc-AFM, respectively.
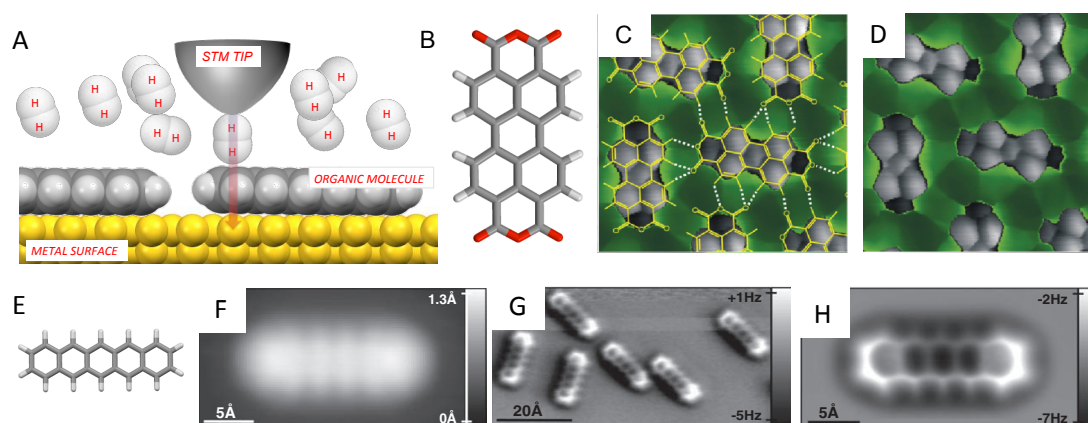

Figure X.2. Schematic representation (A) of the STHM set-up. Molecular structure (B) of the PTDCA molecule (Grey: Carbon, White: Hydrogen, Red: Oxygen). STHM image of PTCDA molecule (C,D) on Au(111) in its herringbone phase (image size 2.5 nm × 2.5 nm) (Reproduced from ref. 35 with permission from The American Chemical Society). Molecular model (E) of pentacene (Grey: Carbon, Whi[...] pentacene on Cu(111) (Repr[...] Science).

The flat [...] STM chamber was [...] dide [...] he STM tunnelling junction with molecular hydrogen was achi[...] %) into the LT-STM (low temperature STM) chamber at a pressure varying between 10^{-9} and 10^{-7} mbar. Using this technique *Tamirov et al.* were able to obtain sub-molecular resolution images of aromatic molecules such as tetracene and 3,4,9,10-perylene-tetracarboxylic-dianhydride, PTCDA, (Figure X.2B). Some representative images of PTDCA as imaged through STHM showing the high level of accuracy are depicted in Figure X.2C-D. The imaging mechanism of STHM is

strictly related to the chemical structure of the molecule itself rather than its electronic molecular states as in conventional STM. The short diatomic molecules (hydrogen or deuterium) act as sensors for short range *Pauli* repulsion from the surface behaving as transducers and transforming these forces into a variation of the tunnelling current. The hydrogen/deuterium probe is therefore responsible for a modulation of the tunnelling current over the conventional LDOS contrast.

The second technique is nc-AFM, a powerful method to achieve atomic resolution of organic molecules on surface.[36] Contrary to STM, which probes the LDOS of the sample for given energies, non-contact Atomic Force Microscopy probes the force between the probe and the sample during scanning. A sharp probe attached to a piezoelectric quartz crystal resonator is raster-scanned over the sample. The AFM image is then reconstructed measuring either the change in amplitude at a constant frequency (amplitude modulation mode) or measuring the change in resonant frequency at constant resonance amplitude (frequency modulation mode). Atomic resolution can be achieved at low temperatures (~5 K) in UHV (ultra-high vacuum) using a nc-AFM equipped with a qPlus® sensor.[37] The qPlus® system is composed of a quartz tuning fork fixed to a support by one of its prongs while the free standing prong holds the probe tip. The fork operates in frequency-modulation mode, at high resonance frequency (approx. 30 kHz), and the signal measured is the shift of the resonance frequency Δf caused by the interaction between tip and sample. As for the STHM case, submolecular resolution can be achieved when the AFM tip is functionalized with a diatomic CO molecule.

Using this technique *Gross* and coworkers were able for the first time to image with atomic resolution the structure of a planar aromatic molecule deposited on a metallic surface.[38] The functionalization of the AFM tip with a CO molecule enables atomic resolution images of individual pentacene molecules, as deposited on both conductive (*i.e.* Cu(111)) and non-conductive (*i.e.* on a NaCl bilayer on Cu(111)) surfaces (Figure X.2F-I). Generally, without tip functionalization, single molecule visualization with AFM is extremely challenging due to the relatively low stability of the system, which is strongly affected by different factors such as the tip structure (*e.g.* its atomic composition and geometrical features) and the occurrence of unintentional molecular manipulation. For this reason, functionalization of the AFM tip apex with a stable molecule adopting a known structure and geometrical orientation (CO is known to bind to the AFM tip by its carbon atom) can both increase the final imaging resolution and facilitate the comparison between experimental results and theoretical calculations. The nc-AFM images of pentacene were obtained using constant height mode while the frequency shift Δf was recorded. Interestingly, all the molecules deposited on Cu(111) displayed local Δf maxima at the edges of the terminal rings near the carbon atom positions and a minima above the central rings of pentacene together with a dark halo completely surrounding their structures (Figure X.2H-I). The origin of this contrast could be explained using DFT simulations that

assigned the high contrast to the Pauli repulsion w[...] [...]
contribute only an attractive background force [...] [...]
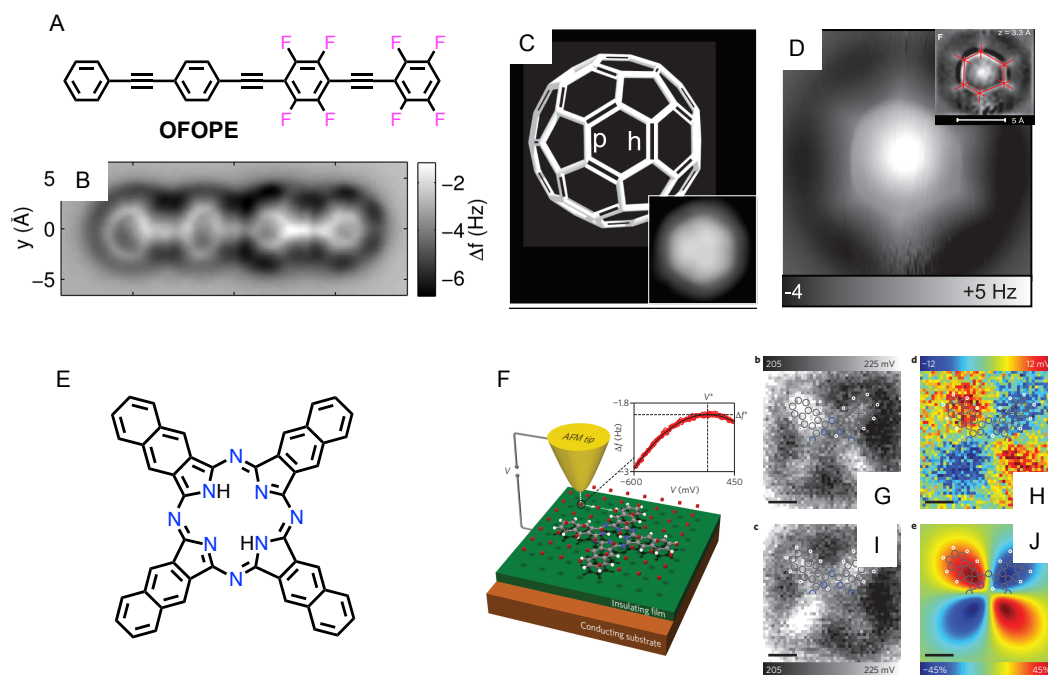molecule.[38, 39]

Figure X.3. Molecular structure (A) of a fluorinated derivative **OFOPE** and its measured constant-height frequency shift Δf image (B) (Reproduced from ref. 40 with permission from the American Chemical Society). (C) Molecular structure of C_{60}, showing the different h (fusing two six-membered rings) and p (fusing a six and a five-membered ring) bonds and a filtered NC-AFM image (D) of C_{60} obtained with a CO functionalized tip at Z=3.3 Å (Reproduced from ref. 41 [...] is[...] from American Association for the Advancement of Science). Molecular structure (E) of naphthalocyanine. Schematic representation (F) of KPFM measurements method on naphthalocyanine: at each point of the grid (marked with the red points) frequency shifts are recorded as a function of the applied Voltage (inset). LCPD mapping of naphthalocyanine as deposited on a NaCl/Cu(111) before (G) and after (I) current induced tautomerisation (scale bars= 0.5 nm). Image obtained after subtracting I to G (H) and DFT calculated asymmetry of the z-component of the electric field at 0.5 nm above the naphthalocyanine (J) (Reproduced from ref. 44 with permission from the Nature Publishing Group).

Following the development and consolidation of this technique, *Moll* and co-workers used nc-AFM with CO-tip to explore the structure of different types of molecules on metallic surfaces. In recent work, they investigate the image distortion characteristic of CO terminated tips and the visualization features of aromatic rings possessing different electronic density.[40] In order to do so, a partially fluorinated *oligo*-phenylene ethynylene (**OFOPE**) was imaged *via* nc-AFM using a CO functionalized tip (Figure X.3A,B). This molecule is comprised of two different subsections featuring hydrogen and fluorine substituted phenyl rings. When imaged by AFM, the fluorinated rings appear to have a considerably smaller diameter when compared to the non-fluorinated phenyl rings. Kelvin Probe Force Microscopy, STM and nc-AFM, in

combination with first principle calculations, revealed that the image distortion of the fluorinated rings can be attributed to their lower charge density in comparison to the hydrogenated ones (a factor 2 smaller as calculated by DFT). This can be rationalized as a consequence of the high electronegativity of the Fluorine atoms that seems to influence the π-electrons of the aromatic rings. Additionally the molecule also appears distorted due to the presence of attractive van der Waals interactions and for low tip height both Pauli repulsion and van der Waals forces tilt the CO probe in a manner that the bonds of **OFOPE** appear much shaper.

The group of *Gross* was also able to show that different bond orders of individual carbon-carbon bonds in planar and non-planar polycyclic hydrocarbons can be visualized and characterized using nc-AFM with CO functionalized tips. Determination of bond order, angle and length can potentially be very useful to predict reactivity, stability and aromatic character of molecules adsorbed on a surface. In their study, *Gross* and co-workers elucidated the bond order of three molecules: two extended polycylic aromatic hydrocarbons (PAH) (namely hexabenzocoronene, HBC, and dibenzo(cd,n)naphtho(3,2,1,8-pqra)perylene, DBNP) and C_{60} fullerene.[41] In the case of C_{60} the bonds fusing two hexagons (h) are structurally different from the bonds fusing a pentagon and a hexagon (p) (Figure X.3C). Indeed, both theoretical and experimental investigations by means of neutron, electron and X-ray diffraction have shown that the bond h is ~ 5% shorter than the bond p.[42, 43] The difference in bond order for p and h is reflected in the constant height AFM with CO functionalized tip illustrated by a characteristic bond length alteration corresponding to the cyclohexatriene motif of the C_{60} structure (Figure X.3D). Two main factors could be deduced. First the local frequency shift Δf is greater at a position above the h bonds. Second the h bond length appears shorter than the corresponding p bond. The increase of contrast localized around the h bond can be interpreted as a consequence of the higher local electron density associated with this bond, which induces a greater *Pauli* repulsion. Using *Laplace* filtered images it was possible to determine the apparent bond length of $L'_h = 2.0$ Å and $L'_p = 2.7$ Å. Notably, both bonds appear to be much longer than what was previously measured by diffraction techniques with a difference of ~30% in the bond lengths as determined by AFM. DFT simulations indicate that the possible reason for the discrepancy between real and observed bond lengths can be attributed to the tilting of the CO molecule on the AFM tip, which makes the h bond appear shifted further away from the molecular center than the p ones. Constant height AFM analysis of the other two hydrocarbons HBC and DBNP qualitatively corroborated the bond order related contrast observed in the case of the C_{60} analysis. It is important to point out that the bond length amplification originating from CO tilting is also the factor that enables the detection of different bond orders, which would be otherwise not visible within the accuracy of the AFM instrument.

Non contact-AFM and STM imaging have also been used in combination with other techniques in order to obtain information about both structure and electronic properties of molecules on surface. Kelvin Probe

Force Microscopy (KPFM) for example has been utilized to probe the charge distribution on an isolated naphthalocyanine molecule (Figure X.3E).[44] This technique can be used to measure the local contact potential difference (LCPD) between the tip and the sample, as a function of the charge distribution on the surface. The investigated naphthalocyanine was deposited on a Cu(111) crystal covered with two monolayers (2ML) of a NaCl island at (5 K). Free base naphthalocyanine can be adsorbed on the surface as two tautomeric forms (depending on the position of the N–H). The interconversion between the two tautomers (representing a switch) can be triggered by a current pulse. A schematic representation of the KPFM measurement as performed on the naphthalocyanine is depicted in Figure X.3F. In this method, a metal terminated AFM tip is scanned along a grid above the molecule and at each intersection of the grid a Δf (V) spectrum is recorded. The position of the maximum of the parabola gave the LCPD value and the frequency shift at compensated LCPD(Δf) for that point. Upon performing this measurement, *Mohn* and coworkers observed a striking asymmetry between the lobe parallel (H-lobes) and perpendicular (N-Lobes) to the inner hydrogen atoms, which it is remarkably clear when subtracting the LCPD data from the initial state and the switched configuration (Figure X.3G-J). Comparison of the electric field generated by the distribution of the total charge to the LCPD has also been performed using DFT simulations. The calculated electric field asymmetry exhibits a similarity to the experimental data obtained by KPFM, leading to the conclusion that the LCPD was indeed reflecting the submolecular charge distribution. In the same work a further increase of the image resolution was obtained by functionalizing the AFM tip with a CO molecule. The contrast of the images in this context was affected strongly by the tip height (z) and as the tip sample distance was decreased, the intramolecular contrast gradually increased. Such drastic increase of resolution in KPFM was ascribed to the close proximity between the tip and the sample. The small oscillation amplitude also contributes to enhance the ability to sense short-range electric fields originating from local charge variations.

Finally, molecular structure resolution using nc-AFM was also recently employed to identify the different components of a very complex mixture of hydrocarbons.[45] Due to its high importance in industry and to its incredible chemical complexity, Asphaltene was chosen as a target mixture. In this context, nc-AFM offers the unique capability to identify and characterize isolated units of a very complex mixture, providing precious insight into the interatomic connectivity. For this experiment, a small coverage (<5 % Monolayer, ML) of Asphaltene molecules was obtained on a Cu(111) crystal partially covered with NaCl islands (2ML) by flash-heating a sample of Asphaltene from a silicon wafer.
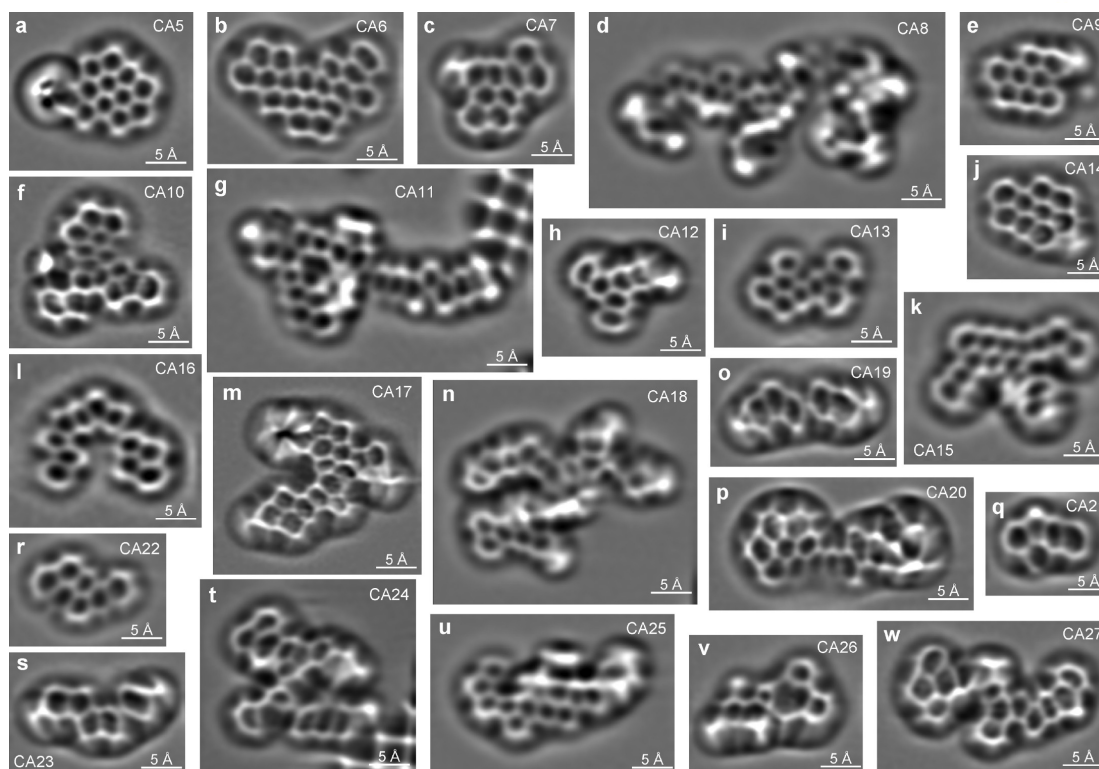
Figure X.4. *Laplace* filtered nc-AFM images (a-w) of different molecular components observed by depositing coal-derived asphaltenes on Cu(111) or on NaCl(2ML)/Cu(111) (Reproduced from ref. 45 with permission from the American Chemical Society).

Using a combination of STM and nc-AFM investigations, the authors found that the main components of Asphaltenes are different types of PAHs bearing peripheral alkyl chains. nc-AFM was able to elucidate the structure and the atomic connectivity of a wide range of Asphaltene components (Figure X.4). Upon focusing their attention on asphaltenes of different origins (coal, and petroleum Asphaltenes), the authors were able to identify structural differences between their respective components.

X.3 Reactivity of Aromatic Molecules on Metallic Surfaces

The incorporation of functional organic aromatic nanomaterials into electronic devices requires the development of tools to assemble highly extended molecular systems with long-range order and atomic precision. Despite the continuous progress in the field, the synthesis of extended nanomaterials based on traditional solution chemistry presents several challenges and limitations. Indeed, PAH featuring extended surface areas and high molecular weight are often characterized by extremely low solubility and processability, which can affect the reaction yield, purification and characterization. Additionally, even in the case of a successful synthesis, complicated transfer protocols are usually necessary during the device fabrication process to deposit these compounds on a substrate support. In this context, the exploitation of surface mediated reactions for the construction of extended organic architectures from reactive small

molecules is a promising approach.[46-49] This bottom-up method generally sees the deposition of an appropriate molecular precursor on a metallic surface in UHV and its subsequent inter- or intramolecular reaction is achieved by the application of a secondary stimulus (*e.g.* temperature gradient, light irradiation or electrical stimulation). This strategy possesses several advantages when compared with conventional solution synthesis. The absence of a solvent not only alleviates solubility requirements, but also allows the use of a wider temperature range (from 5 to 600 K) permitting the investigation of reactivity pathways that are not accessible to classical wet chemistry. Furthermore, the metallic surfaces themselves can participate as a catalyst during the chemical reaction. In this section we will discuss the most important types of surface-mediated reactions that have been used so far to construct complex organic architectures starting from aromatic building blocks, highlighting some of the most relevant examples for each specific reaction class.

X.3.1 Surface Mediated Polymerization

X.3.1.1 Polymerization via Terminal Acetylene Coupling

Reactions involving the exploitation of the intrinsic chemical reactivity of terminal alkyne groups are among the most exploited synthetic tools for the construction of both 1-D and 2-D extended organic structures on surfaces.[50, 51] *Fischer* and *Crommie* recently demonstrated the use of this strategy to assemble a fully conjugated polymer derived from polyacetylene on a metallic substrate.[52] The thermally induced "enediyne cyclization" of a 1,2-bis(2-ethynylphenyl)ethyne precursor **1** gave a diradical intermediate **2**, that polymerizes on the surface via a radical step-growth mechanism (Figure X.5A). Deposition of **1** on a Au(111) surface in UHV at room temperature and subsequent thermal annealing at 160 °C induces two C1-C5 radical cyclization reactions as well as the intermolecular radical recombination that leads to the oligo-(E)-1,1'-bi(indenylidene) derivative **3**. Using a combination of nc-AFM, STM and STS on individual oligomeric chain, it was possible to shed light on both the structure and the electronic properties of each unit. The molecular connectivity of the oligomer was resolved by nc-AFM (Figure X.5B). Theoretical simulations and dI/dV mapping of the oligomers highlighted the presence of an extended electronic state localized along the center of the conjugated polymer backbone (Figure X.5C-D). This electronic structure can be rationalized taking in consideration the electron spatial delocalization caused by the formation of highly extended π-system along the polymer backbone.
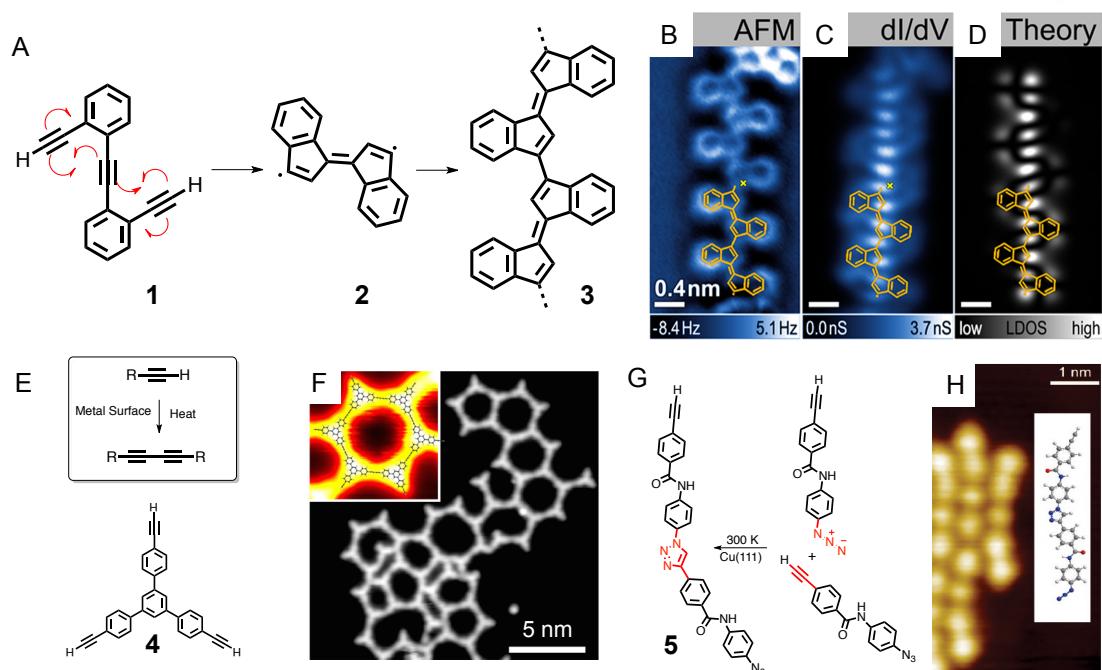
Figure X.5. The C1-C5 cyclization (A) reaction leading to the formation of the diradical intermediate **2** and its oligomers **3** from polyacetylene precursor **1**. nc-AFM (B), *dI/dV* mapping (C) and theoretical simulation (D) of the electronic structure of **3**, showing its atomic connectivity and the presence of an extended electronic state, respectively. (Reproduced from ref. 52 with permission from the American Chemical Society). (E) Surface mediated alkyne dimerization reaction (Top) and structure of the trialkyne precursor **4** (Bottom). STM image (F) of the 2-D network formed by polymerization of **4** on a Ag(111) surface, inset: 3-D model of the network overlayed to the STM image. (Reproduced from ref. 55 with permission from Nature Publishing Group). Surface mediated "Huisgen type" cyclization (G) leading to oligomerization of **5** (in red the functional groups involved into the formation of the triazole ring are evidenced) LT-STM image (H) showing the morphology of the oligomers and their 3D models (inset). (Reproduced from ref. 58 with permission from the American Chemical Society).

Another successful strategy for the preparation of 1-D and 2-D extended aromatic systems in UHV involves the exploitation of the selective reaction of the metallic substrate with functional groups at the Metal-Vacuum interface. This strategy is inspired by the extensive work performed on transition-metal mediated cross-coupling reactions in solution.[53, 54] A representative example is the polymerization of molecular units bearing terminal alkynes. Using this approach, *Zhang et al.* were able to polymerize molecular precursors such as 1,3,5-triethynyl-benzene and 1,3,5-tris(4-ethynylphenyl)benzene **4** through a surface mediated alkyne homocoupling (Figure X.5E).[55] The polymerization of these tritopic precursors was performed by evaporating the isolated molecules onto a Ag(111) surface, followed by thermal annealing at 300 K. This procedure resulted in the highly selective formation of a new C(sp)-C(sp) single bond between the terminal atoms of the alkyne functionality, leading to covalently bonded dimers or highly extended reticular networks. The extended porous network formed via this route was composed of a heterogeneous distribution of pores featuring different sizes and shapes (*i.e.* pentagon, hexagon, heptagon, Figure X.5F). Such observation can be attributed to the inherent flexibility of the molecular precursors and to the irreversibility

of the homocoupling reaction. Interestingly, when a similar experiment was performed by the group of *Fasel* using an Au(111) surface a drastic change in reactivity of the terminal acetylene functionality was observed. Rather than undergoing homocoupling reactions the terminal alkynes underwent a [2+2+2] cyclotrimerization to form 2-D networks.[56] Further investigations on the reactivity of terminal acetylene, showed the possibility to use this group as partner in a [3+2] cycloaddition reaction with appropriately functionalized azide derivatives.[57, 58] Due to the possibility to perform heteromolecular coupling on surface, this discovery strongly increases the applicability of these systems, extending the use of this chemistry to the construction of more complex architecture formed by different functional and structural units. *Fuchs* and co-workers were able to induce the oligomerization of monomer **5** at room temperature by depositing it on a Au(111).[58] Exploiting the interaction with the surface the triple bonds and the azide functionality of **5** reacted in a 1,3-dipolar cycloaddition leading to the exclusive formation of the 1,4-substituted triazoles (Figure X.5G-H). The success of the coupling reaction and the formation of oligomeric species was confirmed by STM (Figure X.5H) and showed the structure and connectivity of single oligomeric chain.

X.3.1.2 Polymerization of Halogenated Precursors

One of the most common strategies used to assemble extended aromatic systems from small molecular precursor relies on the use of halogenated molecular precursors.[59-63] The coupling of these molecular units is achieved by deposition of the halogenated precursor on a metallic surface followed by subsequent heating of the underlying substrate. The thermal annealing of the surface induces reactions (*e.g.* surface mediated *Ullmann* coupling) that link isolated molecules into higher ordered 2-D structures.

One of the most important parameters dictating the reactivity of molecular precursors on surfaces is the type of halogen substituent. Differences in the bond dissociation energies (BDE) of the C–X bond (336 kJ mol^{-1} for Br–C_6H_5 and 272 kJ mol^{-1} for I–C_6H_5 in the gas phase)[64] are reflected in the reactivity of these groups on surfaces. During the thermal annealing process, iodinated precursors have been shown to react at lower temperatures than brominated analogues. In their pioneering work, *Grill* and co-workers were able to exploit the difference in reactivity between C–I and C–Br bonds with the goal to produce multiple nanostructures in a hierarchical manner from a tetra-halogenated porphyrin **6**, which bears two iodophenyl and two bromophenyl substituents in the 5, 15 and 10, 20 positions, respectively (Figure X.6A).[65] Deposition of the monomer on a Au(111) surface held at 80 K resulted in the adsorption of intact molecular units containing both iodine and bromine atoms. Thermal annealing of **6** at room temperature induced the cleavage of the C–I bond and a radical recombination to give covalently linked dimers of **6**. Further annealing to 120 °C induced an efficient polymerization of **6** by selective and complete activation of the residual C–I bonds. Due to the "*trans*-like" arrangement of the iodine atoms, the polymerization reaction leads to the formation of linear oligomer chains (Figure X.6B). The substantially lower activation temperature of the C–I bond in

respect to the C–Br bond, allowed the complete preservation of the bromine atoms on the oligomers allowing further growth of this structure. Annealing of the oligomers at 250°C, induces the dissociation of the C–Br bond leading to the growth of a highly regular 2D architecture (Figure X.6C). The same principle has been demonstrated to grow heterogeneous networks formed by multiple types of units. Introduction of a secondary component in the system (*i.e.* a dibrominated oligofluorene) has been shown via STM to lead to the formation of hybrid structures composed of interconnected porphyrin and fluorene oligomers
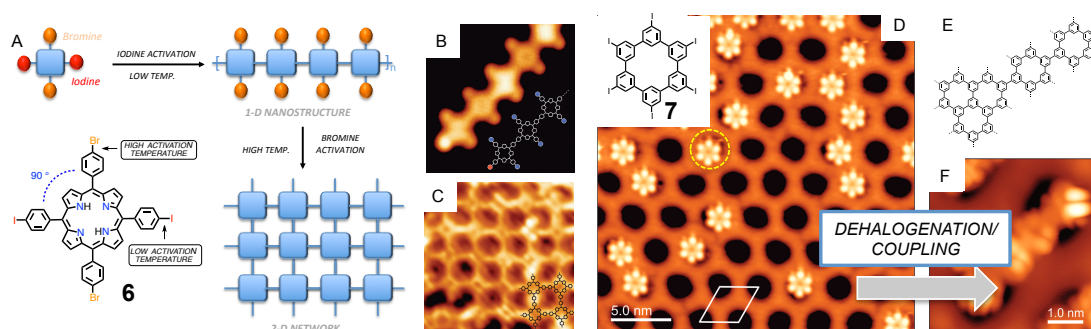
.

Figure X.6. Schematic representation (A) of the hierarchic construction of 1-D and 2-D nanostructure starting from the tetrahalogenated porphyrin **6**. Upon selective activation of C-I bond at 120°C the 1-D polymerization of molecule **6** can be triggered. Further increase of the temperature to 250°C induces the activation of the C-Br bonds and the interconversion of the 1-D nanostructures into extended 2-D networks. LT-STM images of the 1-D oligomers (B) and of the 2-D networks (C) (Reproduced from ref. 65 with permission from Nature Publishing Group). LT-STM image of molecular precursor **7** as deposited on a BN surface (inset: molecular structure of **7**). Generic representation (E) of the structures obtained by the coupling of **7**, and corresponding LT-STM (F) of some of the networks obtained (Reproduced from ref. 66 with permission from The American Chemical Society).

A further advancement on this technique has been recently demonstrated by the group of *Gröning* and *Dienel*, which showed the possibility to perform this coupling on an insulating surface.[66] Since non-conductive surfaces are required as support material for electronic devices, the investigation of the reactivity of isolated molecules on insulating surface remains an important challenge in nanoscience. In their experiments, *Gröning* and coworkers used an isolating Boron Nitride (BN) monolayer supported on a Rh(111) surface (Figure X.6D). The reactivity of hexaiodinated precursor **7** on the highly corrugated BN surface during thermal annealing showed a wide temperature range from the start of the dehalogenation process (500 K) to the full dehalogenation and coupling of the isolated molecules (800 K) (Figure X.6E-F). This observation is distinctive from the results commonly observed on metallic surfaces and the behaviour of the same molecule in the gas-phase. A combination of STM investigation and DFT simulation showed that the interaction of the BN with the molecule itself governs the dehalogenation process.

X.3.1.2 Polymerization through Dynamic Covalent Chemistry

In recent years the concepts of dynamic covalent chemistry (DCC) using aromatic building blocks have been successfully applied to the creation of organic architectures on a variety of surfaces.[67-72] As opposed to the previous examples the intrinsic nature of the interactions exploited (*e.g.* high reversibility, high thermal stability and slower kinetics of bond cleavage/formation), the structures formed under these conditions are mainly guided by the thermodynamics of the process. The thermodynamic driving force combined with the reversible covalent nature of the interaction paves the way for the assembly of architectures featuring long-range order and higher stability when compared to non-covalent interactions. Among the different reactions that have been developed in this field, imine condensation and the esterification of boronic acid have been exploited the most for the creation of organized networks on surfaces.[73-76]
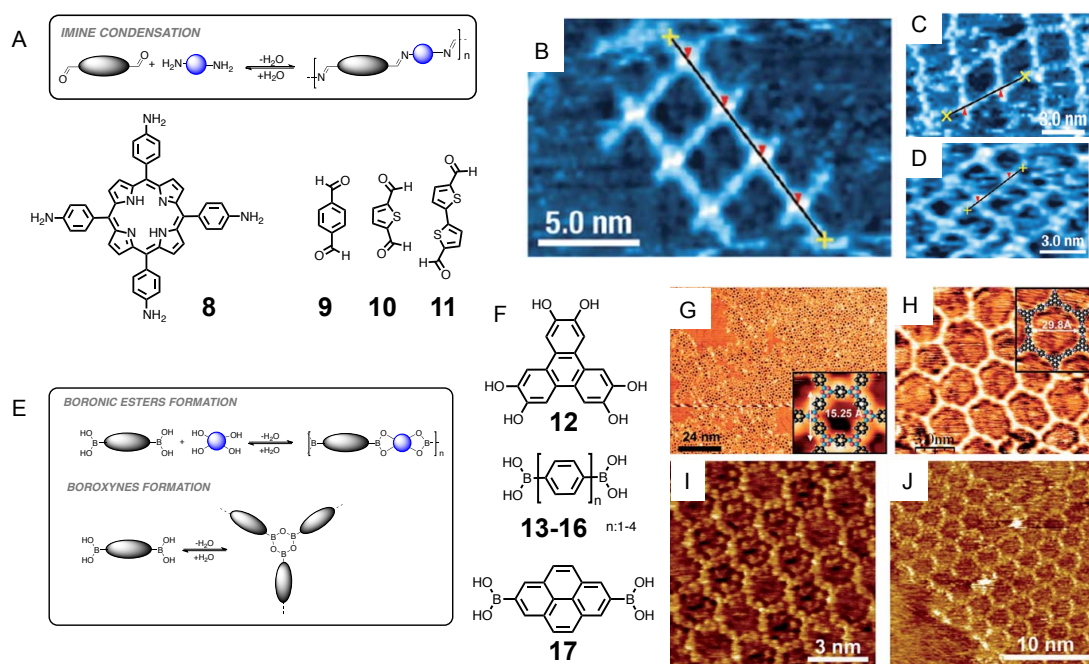
Figure X.7. (A) The imine condensation reaction (top) and the tetramino porphyrin **8** with the partner dialdehydes **9-11** (bottom). Representative STM images (B-D) of 2-D networks formed by the condensation of **8** with **9**, **10** and **11.** (Reproduced from ref. 77 with permission from the American Chemical Society). Esterification of boronic esters (E) and their self-condensation into boroxines. Triphenylene derivative **12** and diboronic acids **13-17**. STM image (G) of 2D networks formed by self-condensation of **13** on Ag(111) surface and with triphenylene derivative **12** as obtained by *Abel* and coworkers (inset: network structure as obtained from DFT)(Reproduced from ref. 78 with permission from the American Chemical Society). Representative STM images (I and J) of isoreticular networks that can be formed using different diboronic acids (**13-17**) on HOPG, in particular network obtained by self-condensation of **14** (I) and **15** (J) are depicted. (Reproduced from ref. 79 with permission from the American Chemical Society).

One example of the use of imine condensation for the creation of 2-D aromatic macrostructures on surfaces is shown in Figure X.7A-D. *Kunitake* and coworkers were able to prepare a variety of organic networks by

exploiting the condensation reaction between the tetraminoporphyrin **8** and a library of linear dialdehydes **9-11** (Figure X.7A).[77] Simple mixing of molecule **8** (which presents a disposition of its amino group at 90° one from each other) with the appropriate linear dialdehyde under thermodynamic control leads to the formation of various extended networks. Deposition of this aqueous solution onto a Au(111) surface and in situ STM indicated the formation of 2-D frameworks with different geometries and pore sizes, strictly dependent on the structural parameters and the configuration of the dialdehyde used (Figure X.7B-D).

Another tool that has been exploited for the assembly of 2-D covalent architectures on surface is the chemistry of boronic acids. To date both the reversible formation of boronic esters and cyclic anhydrides (boroxine) have also been used to create extended porous aromatic frameworks on surfaces. In the particular case of boroxine, the general reaction scheme involves the participation of three molecules of boronic acid which upon condensation and elimination of three H_2O molecules, form a very stable six-membered ring characterized by alternating boron and oxygen atoms (Figure X.7E).

This approach has been successfully used by *Abel* and coworkers to prepare extended 2-D networks starting from the commercially available 1,4-benzenediboronic acid **13**.[78] Upon sublimation of benzenediboronic acid under ultrahigh vacuum (UHV) conditions onto a clean Ag(111) surface (kept either at room temperature or at 400 K), 2-D extended hexagonal networks were formed (Figure X.7G). The same principle has been used by the authors to couple different types of molecule through an esterification reaction. Indeed, when 1,4-benzenediboronic acid was co-sublimed together with triphenylene derivative **12** on Ag(111), the formation of another 2-D hexagonal network with pores consistently larger than the previous one (29.8 Å versus 15.25 Å) was observed. Additionally, the comparison between the two networks shows the presence of fewer local defects in the last one. This can be rationalized considering that the boronic acid esterification is a bimolecular reaction and therefore follows a more favourable kinetic pathway in comparison with the trimolecular boronic acid self-condensation.

A further example that shows the multivalent application of boronic acids on surface is the work of *Lackinger* and co-workers, which were able to obtain a series of isoreticular networks inducing the dehydration of aromatic diboronic acids featuring different lengths on HOPG.[79] By employing a library of diboronic phenyl acids featuring different lengths and structures (diacids **13-17**, Figure X.7F), the authors were able to prepare a series of 2-D covalent frameworks in which the lattice parameters and pore sizes could rationally be designed by using the desired type of acid (Figure X.7I,J).

X.3.2 Cyclodehydrogenation Reactions

Cyclodehydrogenation reactions have been extensively used in the last decades in order to obtain synthetic access to extended PAH using solution-based chemistry. Among the different sets of conditions, *Scholl* and

Kovacic reactions, which use Lewis acids/oxidants combinations (such as for example FeCl₃, AlCl₃, Sc(TfO)₃, or TfOH), have proven to be very efficient to induce intramolecular cyclodehydrogenation process.[80-83] Unfortunately, due to the harsh conditions used, these reactions are generally characterized by a low degree of functional group tolerance and by the presence of undesired side reactions (*e.g.* chlorination, intermolecular coupling and transposition reactions).[81, 84-87]

With the advent of STM as a characterization technique, the possibility to induce the cyclodehydrogenation reaction on a metallic surface has also been thoroughly investigated. Over the years different protocols have been established in order to prepare extended aromatic structures on surfaces, the conditions of which are strictly dependent on the type of metal surface and molecular unit used. One of the most reliable approaches involves the deposition of a geometrically pre-organized molecular precursor on a metallic surface followed by thermal annealing of the substrate at temperatures in the range between 300-400°C. An *in-depth* investigation of the cyclodehydrogenation process on metal surface was performed by *Fasel* in 2011.[88] In this study, triangular oligophenylene **18** was deposited on a Cu(111) surface and gradually annealed to 200 °C. Through the combined use of STM and *ab initio* DFT simulations, it was possible to identify and characterize the intermediate states leading to the formation of the fully cyclized nanographene **19** (Figure X.8A-C). In total, a six step mechanism featuring five different intermediates was found to be necessary for the complete cyclodehydrogenation of **18**. The authors conceptualize this complex mechanism by dividing it into three consecutive simpler processes: (i) Cu mediated radical C–H bond breaking, (ii) rotation of the *p*-phenylene towards the neighbouring unit and formation of a new C–C bond by radical addition with consequent loss of the H atom and (iii) recombination of the H atoms. Two of the intermediates composing this mechanism were stabilized by the interaction with the surface and their structural characterization was performed via STM. As evidenced by this work, one of the most important advantages of surface mediated intramolecular cyclodehydrogenation consists of the ability to precisely control the atomic connectivity and the edge structure of the resulting nanostructure by appropriate design the molecular precursor.

Following the same approach, *Fischer* and *Crommie* were able to synthesize peripentacene (**21**), using a thermally induced cyclodehydrogenation reaction on Au(111).[89] From the structural point of view, peripentacene, which belongs to the class of molecules known as *n*-periacenes, consists of two linear pentacene units fused at the peri-position in a rectangular PAH.
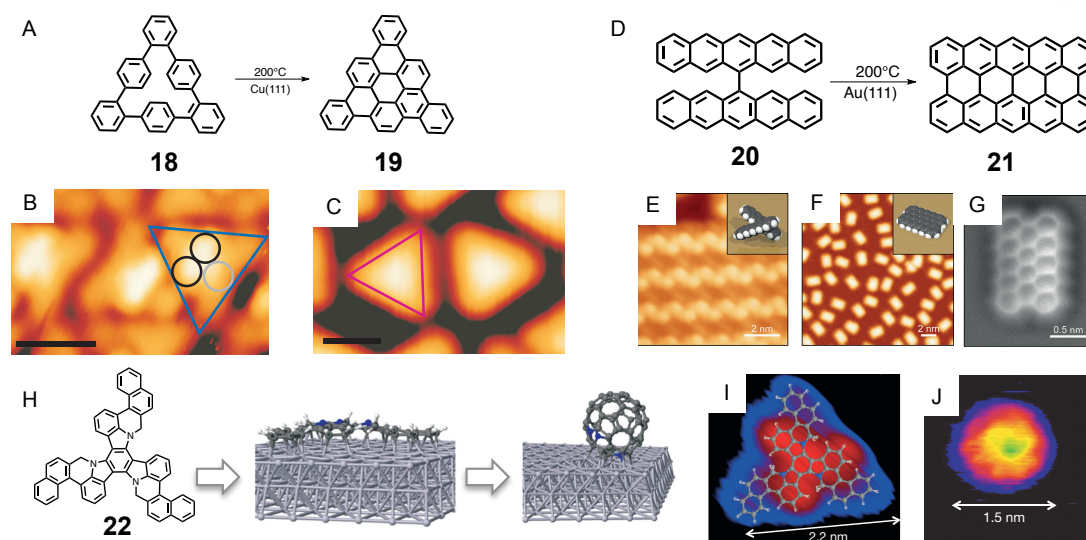
A ... 18 → (200°C, Cu(111)) → 19

D ... 20 → (200°C, Au(111)) → 21

Fig. ... Cyclodehydrogenation ... deposited on Cu(111) (B) and after heating at 200°C (C), showing the increase of planarity in the molecule (Reproduced from ref. 88 with ... from ... when ... to ... from 6,6'- ... Au ... 6,6 ... perip ... ed from the ... s ... lec ... ef. 89 with permission from Wiley-Verlag GMBH). Cyclodehydrogenation (H) leading to the formation of triazafullerene from molecular precursor **22**. STM image (I) of **22** as deposited on the Pt(111) surface, with its molecular structure superimposed and after annealing (J) the surface at 750 K. (Reproduced from ref. 94 with permission from The Nature Publishing Group)

Its characteristic structure exhibits two parallel long edges with zig-zag configuration and two short armchair edges. Despite several attempts to synthesize this molecule using traditional solution based chemistry, fully cyclized peripentacene has been an elusive target and could never be isolated.[90, 91] The great difficulty related to its synthesis is strictly connected to a combination of factors, such as its low solubility, its thermal and photochemical instability, and its predicted antiferromagnetic ground state.[92, 93] *Fischer* and *Crommie* employed a strategy that exploits the direct on-surface-synthesis of peripentacene from the molecular precursor 6,6'-bispentacene **20** via a thermally induced cyclodehydrogenation reaction. Precursor **20** is constituted by two pentacene subunits linked at the C6 position arranged in an orthogonal conformatio ... ntacene **21** from **20** was obtained by thermal annealing at 200°C on a Au(11 ... STM (7K) showed the formation of a submonolayer of isolated molecular e ... ctures with width, length and height comparable to the expected dimensions ... -F). The unambiguous structural identification of peripentacene was confirm ... indicating the efficacy of this method to provide access to exotic aromatic co ... le through conventional solution chemistry.

Surface me ... an also be exploited for the construction of 3-D hydrocarbon structure. One of the most remarkable examples in this context is the work performed by *Otero* and co-

workers on the synthesis of C_{60} and *N*-Doped C_{60} from molecular precursors.[94, 95] In a typical example, deposition of precursor **22** on a Pt(111) surface followed by subsequent sample annealing at 450 °C induced the surface reaction which yields the corresponding triazafullerene (Figure X.8H). STM analysis of precursor **22** shows a triangular shape and a total apparent height of about 0.14 nm (Figure X.8I). Following annealing of the substrate to 450°C, a drastic change in the morphology of the adsorbate is observed showing the formation of spherical molecules with a height of 0.38 nm and a diameter of 1.5 nm (Figure X.8J). The reduced height of the cyclized compound in combination with XPS data showing a chemisorption process directed by a N–Pt bond indicated a very strong interaction between the fullerene and the Pt(111) which could be at the origin of the high efficiency of this cyclization process.

X.3.3 Metal-Coordination Reactions

Metal coordination reactions are a powerful tool to organize organic aromatic molecules into complex architecture on surface. A pivotal prerequisite for the construction of ordered architecture on a metal surface is an appropriate molecular design of the precursor which among other things should take in consideration the type of metal, the binding geometry and the type of ligand to be used. The types of ligands that have been used most extensively so far to construct metal-organic architectures on surfaces are hydroxyl groups, carboxylates, carbonitriles and pyridine moieties. Combination of these functionalities with the appropriate metal centres (generally Cu, Co, Au or Fe), the proper control of the environment conditions and of the surface used, has originated a wide plethora of 1-D and 2D nanostructures on surfaces.[96-98]
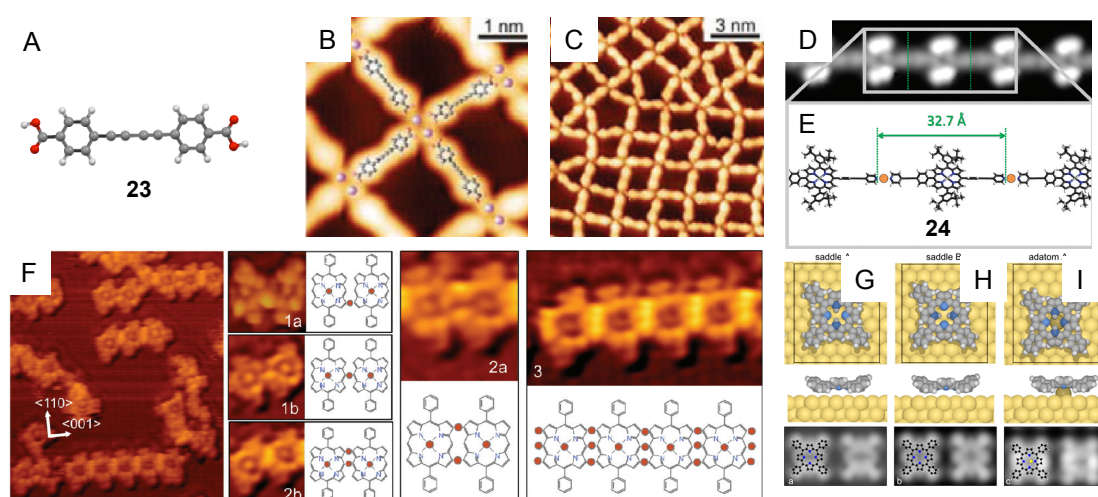
Figure X.9. Chemical structure (A) of benzoic acid derivative **23** (H, white; C, gray; O, red). Representative STM images (B, C) of the **23**-Fe MOCNs on Au(111). Structural node (B) with the central di-iron binding motif represented and large-scale image (C) showing the different polygonal assemblies composing the network (Reproduced from ref. 99 with permission from the American Chemical Society). STM image (D top) of a straight segment of the coordination polymer formed by porphyrin **24** on Cu(111). Graphic representation (D bottom) of the linear pyridyl-Cu-pyridyl arrangement connecting two porphyrins **24** (Reproduced from ref. 107 with permission from the American Chemical Society). Representative STM (E) images showing the variety of linear

metal-organic arrays obtained by thermal annealing of diphenylporphyrins on a Cu(110) surface at 620K(Reproduced from ref. 108 with permission from the American Chemical Society). Calculated adsorption geometries (top and middle) and simulated STM images (bottom) of the two trans tautomers of free-base **TPP** (E and F) and of a **TPP** molecule (G) featuring a Gold adatom in its macrocycle. (Reproduced from ref. 110 with permission from the American Chemical Society)

From the structural point of view, one of the most versatile classes of aromatic molecules that can serve as an organic building block for the construction of extended 1-D and 2-D networks on surface are constituted by the derivatives of benzoic acid. In particular dibenzoic acids due to their favourable geometry (which can allow the disposition of carboxylic moieties at 60, 120 and 180°) and to their synthetic accessibility and tunability are one of the most useful ligands for the construction of 2-D networks on surface. The group of *Kern* reported a classic example of molecular organization of organic molecules based on carboxylic acid derivatives. He reported the synthesis of extended two-dimensional metal−organic coordination networks (2-D MOCN) based on the coordination events between 4,4'-di-(1,4-buta-1,3-dynyl)benzoic acid **23** and Fe atoms on both Ag(111) and Au(111) surfaces (Figure X.9A-C).[99] LT-STM images showed that when a 1:1 mixture of **23** and Fe atoms were deposited simultaneously through organic molecular beam epitaxy on Au(111) or Ag(111) surface the formation of a fully reticulated network was observed (Figure X.9B-C). The newly formed 2-D MOCN was covering homogeneously the entire surface, showing a high degree of insensitivity to the microscopic surface feature such as step-edges, terraces and other defects. High-resolution STM imaging revealed that each network node was comprised of four units of **23** coordinated through their carboxylate functionality to two Fe adatoms. In this configuration two-carboxylate units bind the iron centres in a symmetric manner while each of the other two axial ligands forms bidentate bonds to one Fe atom.[100] As clearly visible from Figure X.9C the MOCN features a high degree of conformational and geometric flexibility, which originates different types of polygonal assemblies such as square, triangles and pentagons. Such diversity in orientation and framework structure was ascribed to the high conformational flexibility of the butadyine backbone. The authors consider such flexibility as the crucial factor conferring the high degree of substrate-error tolerance, which enables the construction of these large 2-D architectures.

Porphyrins are another important class of aromatic molecules, which has been extensively used as molecular building blocks for the construction of metal-organic architectures. Indeed, due to their peculiar structural properties (large π-surface, flat structure and high electron density and ease of sublimation) and potential application (*e.g.* light harvesting, catalysis, optics and nanoelectronic components), the possibility to construct porphyrin-based nanoarchitecture has become a field of tremendous investigation.[101] In this respect, several examples have emerged in which porphyrins peripherally decorated with appropriate ligands (such as nitrile and pyridine) have been organized on a metal surface using coordinative interactions.[102-106] In this context, the groups of *Barth* and *Bonifazi* were able to synthesize the first example of a 1-D

coordination polymer featuring pyridyl-functionalized porphyrins as organic repetitive unit.[107] The repetitive units for this assembly, porphyrin **24,** bear two different types of substituents at its *meso* positions: two phen-1,4-diyl-ethynyl-pyridyl (at the position C5 and C15) and two 3,5-di-tert-butylphenyl (at the C10 and C20 sites). Such structure leads to a linear alignment of the pyridyl group, which are involved in the coordination event. Additionally, the presence of triple bonds bridging the pyridines to the main porphyrin core allows a certain degree of flexibility. Upon deposition of **24** on Cu(111) or Ag(111) surfaces, the formation of metal-organic polymeric assemblies with high degree of flexibility was observed by STM imaging (Figure X.9D). Despite not being able to directly visualize the Pyr-Cu-Pyr coupling motif due to electronic effects, a measure of the distance between two N-atoms of subsequent pyridine moieties shows a spacing of 3.6 Å which is in good agreement with the presence of two metal-organic bonding interactions with a Cu–N distance of 1.8 Å (Figure X.9D). The extreme flexibility that these metal-organic polymers displayed both on Cu(111) and on Ag(111) can be rationalized taking in consideration the enantiomeric conformation that the single units of **24** adopts along the chain. Manipulation experiments performed on isolated oligomeric strands of **24** showed the possibility to move and reversibly relocate the termini of the metal-organic assemblies, proving in this way their great mechanical stability and the high intrapolymer cohesion obtained through the Cu–N bond.

A very recent example of a monodimensional metal-organic architecture formed by porphyrin was provided by the group of *Amabilino*.[108] Using a library of meso-free porphyrins *Amabilino* and co-workers were able to construct 1-D metal organic co-assemblies by employing a process driven by C–H bond scission and the incorporation of Cu atoms in between the organic components (Figure X.9E). Upon sublimation of the porphyrin on a Cu(110) surface and annealing at 380 °C, long and regular linear chains, formed parallel to the [001] symmetry axis of the surface. Combined STM investigations DFT simulations and Temperature Programmed Desorption (TPD) experiments indicate that up to three Cu atoms are incorporated of at the *meso* free and beta positions on opposite sides of the porphyrin macrocycle, leading to highly regular linear arrays. Interestingly, TPD experiments showed that when free base porphyrins were used it was also possible to incorporate Cu atoms into the porphyrin macrocycle leading to an even further degree of structural complexity in the final nanostructure. It is noteworthy, that this peculiar surface mediated reactivity has no precedent in solution-based chemistry and therefore contributes to the development of novel synthetic routes for the construction of organometallic materials.

In the particular case of porphyrins, together with the construction of extended 1-D and 2-D architectures on surface great interest has been dedicated by different groups to the investigation of porphyrin metallation mechanism upon confinement on metallic surfaces.[109] Indeed, such process constitutes a valid methodology to selectively tune and modify both the electronic and the structural properties of this family of compounds once deposited on metallic surface.

In one of the latest efforts on this subject, the group of *Grill* was able to shed some further light on the interactions between tetraphenylporphyrin (**TPP**) and the gold adatoms present on an Au(111) surface.[110] Their combined STM–DFT study indicates that the presence of native gold adatoms on the Au(111) surface can induce a characteristic change in the LDOS of the porphyrins if the adatoms adsorb underneath and coordinate to it (Figure X.9F-H). Prior to this study, the different appearance of isolated **TPP** molecules on Au(111) surface was attributed to the difference in conformation adopted by the TPP once adsorbed on the metal surface. However, both DFT simulation and STS on isolated **TPP** molecules indicated that the apparent increase of molecular height (and increase in brightness) of some of the molecules was instead due to an electrostatic shift of the adsorbate-induced electronic states due to the presence of a gold adatom underneath the porphyrin macrocycle. Further experimental evidences of this theory were obtained by creating single adatoms on the Au(111) surface by STM tip-indentation in proximity of a molecular island of **TPP**. As a consequence of this manipulation, an increase in the number of bright **TPP** molecules was found on the same island. Comparable results were also obtained by lateral manipulation of one of the bright **TPP** detaching of the Au(111) adatoms in a reversible manner and inducing a drastic change in both the brightness of the porphyrin and in its STS spectra.

X.3.3 Graphene Nanoribbon Synthesis

In the last decade, graphene has risen as one of the most interesting nanomaterial due to its peculiar electronic, magnetic and optical properties.[111-115] Unfortunately, graphene exhibits semimetallic behaviour at room temperature, therefore its applications in semiconductor devices has been so far limited. On the other hand, monodimensional confinement of graphene into narrow ribbons (<10 nm) opens a band-gap in graphene.[116-119] Precise manufacturing of Graphene Nanoribbons (GNRs) has become a topic of tremendous interest. Due to the extremely small width (<10 nm) necessary for a meaningful band gap to emerge in GNRs, surface-mediated bottom-up synthesis from molecular precursors has become one of the most promising synthetic routes.

Both theoretical and experiment works showed that the edge structure and width of GNRs are intimately linked with their electronic structure (Figure X.10A-B).[117, 120] In this context, straight GNRs featuring armchair edges (AGNRs, Figure X.10A) should exhibit width-dependent semiconductor behaviour. On the other hand, zigzag GNRs (ZGNR, Figure X.10A) are predicted to possess semimetallic behaviour and spin-polarized edge states.[121-123] Additionally, more complex GNR backbones, such as chevron and cove-type GNR (Figure X.10B), have been designed and produced by surface-mediated synthesis and have been predicted to have interesting electronic, thermoelectric and optical properties..[124-126] To date, modulation of

GNR width, edge structure and geometrical parameters using molecular precursors has been successfully utilized in order to tune their electronic properties.
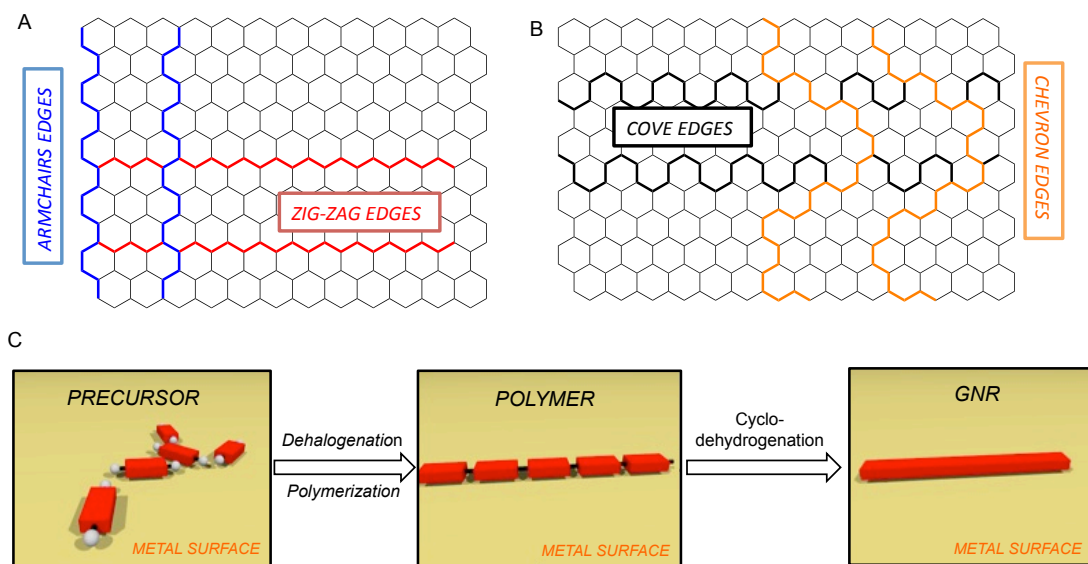

Figure X.10. Schematic representations (A-B) of some of the different edge structures of atomically precise GNRs present in the literature. Schematic representation (C) of the process used for the synthesis of GNR on metal surface. An halogenated molecular precursor is deposited on a Metal surface (step 1) and thermally annealed to induce the C-X bond homolytic cleavage with consequent step growth polymerization (Step 2). Finally, thermal cyclodehydrogenation of the resulting polymer (Step 3) lead to the formation of the GNR.

The typical procedure for the preparation of GNRs through surface–mediated synthesis is depicted in Figure X.10C. In the first step, an appropriatly designed halogenated precursor is deposited on a metal surface (*e.g.* Au, Ag or Cu) and subsequently heated to induce the homolytic cleaveage of the C–X bond. In the following step, the diradical species formed are free to diffuse on the metallic surface and polymerize through a step-growth radical polymerization. Total graphitization of the resulting polymer is then achieved by thermally induced cyclodehydrogenation reaction, which leads to the final GNR structure. The first example of atomically precise GNRs produced by surface-mediated synthesis was provided by the groups of *Mullen* and *Fasel* in 2009.[127] In their pioneering work, the authors used two different types of halogenated molecular precursors to prepare the very first examples of ultranarrow armchair (AGNRs) and chevron type GNRs. Preparation of 7-AGNRs (where 7 is the number of carbon atoms composing the width of the GNR) was achieved using 10,10'-dibromo-9,9'-bianthryl **25** as a dihalogenated precursor (Figure X.11A-C). In a typical experiment (Figure X.11A), deposition of **25** on an Au(111) or Ag(111) surface held at 200°C induced the homolytic cleavage of their halogen atoms and the formation of surface stabilized diradical monomers. The biradical species are able to diffuse across the surface and undergo radical step-growth polymerization to form linear polyanthrylene oligomers (***poly*-25**). Finally, a surface-assisted thermal cyclodehydrogenation at 400°C completes the graphitization of the whole structure, establishing an extended

aromatic system. STM images of the polyanthrylene oligomers obtained (Figure X.11B) shows alternating protrusions with a periodicity of 0.86 nm, in agreement with the periodicity of the bianthryl core (0.85 nm). Such configuration of the polymeric chains is dictated by the steric hindrance between the hydrogen atoms in the *peri*- position of adjacent anthracene units, resulting in the periodic tilting of successive anthracene units with respect to the metal surface. 7-AGNR preparation was then completed by annealing the sample at 400°C, which induced the intramolecular cyclodehydrogenation of the polymeric chains. STM imaging and simulation revealed that the resulting 7-AGNRs possess half the periodicity of the polymeric chains (0.42 nm) and a consistent reduction of their apparent height of 0.18 nm.
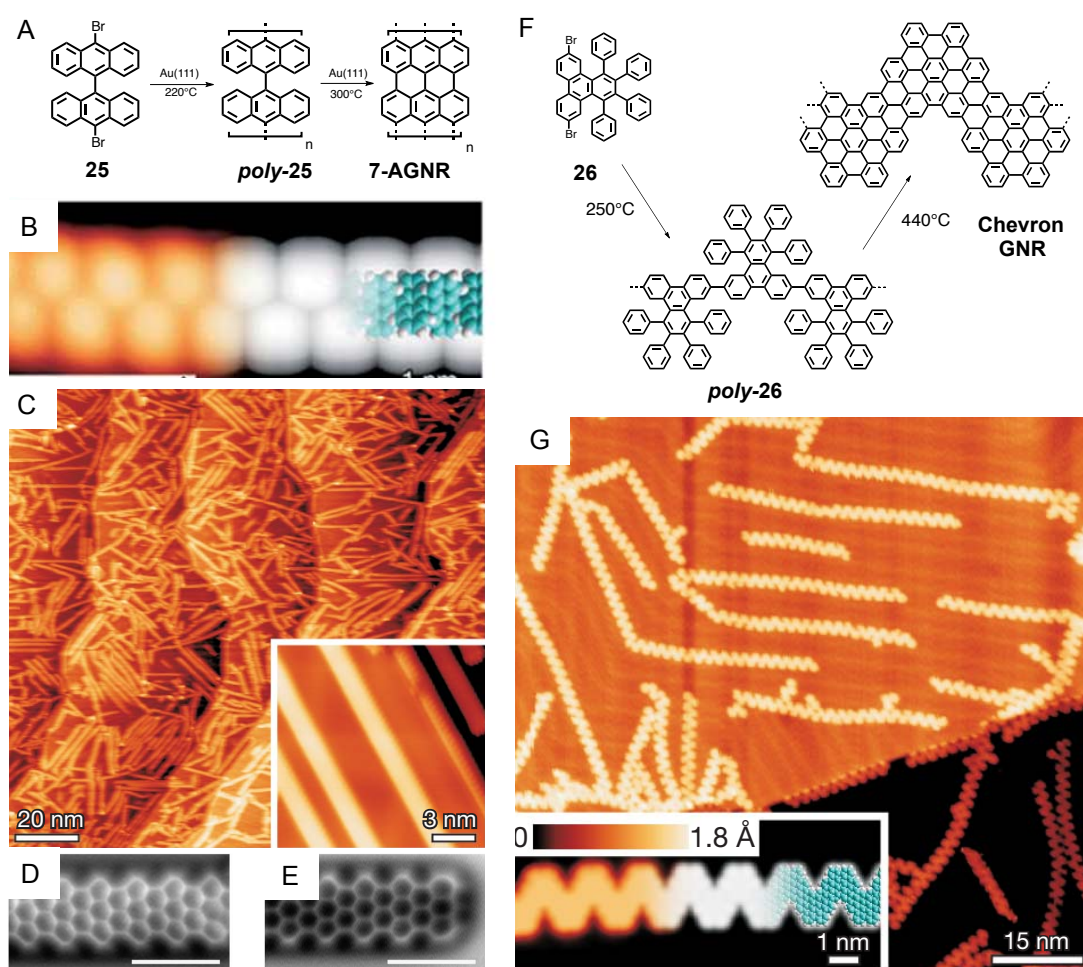
f **7-AGNR** from precursor **25**. LT-STM topography (B) of an isolated polyanthrylene chain (***poly-25***) on Au(111), its DFT-based simulation (right) and an overlaid model of the polymer (blue, carbon; white, hydrogen). LT-STM (C) of **7-AGNR** as obtained after cyclodehydrogenation on Au(111) at 400°C. (Reproduced from ref. 127 with permission from The Nature Publishing Group). nc-AFM image of the side (D) and the termini (E) of **7-AGNR** (Reproduced from ref. 135 with permission from The Nature Publishing Group). Surface mediated synthesis (F) of chevron GNRs from precursor **26.** LT-STM (G) of Chevron GNR on Au(111). Inset STM image of an isolated chevron GNR (left) its DFT simulation (middle) and 3D-model (right) (Reproduced from ref. 127 with permission from The Nature Publishing Group)

When the same process was applied to tetraphenyltriphenylene precursor **26**, chevron-type GNRs were obtained (Figure X.11F-G). In this case, colligation of the dehalogenated monomers on Au(111) was performed at 250°C, yielding oligomeric chains that were fully cyclodehydrogenated into GNRs by further heating at 440°C. STM imaging showed that the resulting chevron GNRs possessed a periodicity of 1.70 nm and an armchair edge structure (Fig. 11G).

Inspired by this pioneering work, interest in surface mediated synthesis of GNRs has greatly expanded.[128-134] The **7AGNRs** structure and interactions with the metal surface was elucidated by the groups of *Swart and Liljeroth*.[135] Using a CO functionalized tip, the authors were able to achieve atomically resolved nc-AFM images of isolated **7-AGNRs**, as obtained from the procedure previously reported by *Fasel* and co-workers. Consistently with the previous STM investigations, constant-height AFM imaging showed GNRs featuring regular armchair edges, alternating rows of two and three fused benzene rings and zig-zag termination at both ends of the GNR (Figure X.11D-E). This highly sensitive imaging method was able to resolve structural defects (despite their very low amounts) that were not possible to visualize by conventional STM, underlining the importance of acquiring both STM and AFM data to comprehensively understand the structure of these complex nanomaterials. Additionally, the authors were able to contact an isolated GNR to the gold substrate by single atom chemical bonding. The selective chemical bonding was achieved by removing the hydrogen atom located at one of the zigzag ends by locally applying a high voltage pulse. Combined nc-AFM and STM showed that the direct GNR-Metal bonding was not affecting the bulk electronic structure of the **7-AGNR** but was instead causing a very strong suppression of its electron–vibron (e–v) coupling.

Computational studies have also pointed out the crucial role of the metal surface in the mechanism of GNR formation, especially during the cyclodehydrogenation process.[136] DFT level transition-state calculations on the cyclodehydrogenation reaction mechanism of **7-AGNRs** showed that the Au(111) surface is acting as a catalyst during this crucial step. Indeed, the most favourable reaction pathways calculated showed the concerted transfer of two hydrogen atoms from the anthracene moieties to the gold substrate, followed by a separate desorption in the vacuum and the formation of a new C–C bond. The cyclodehydrogenation reaction was predicted to be most likely to occur initially at one of the termini of the polyanthryl oligomer and to propagate in a domino-like fashion throughout the polymer backbone.

A general strategy, which has been used to tune the electronic structure of GNRs involves doping GNRs with heteroatoms, leading to the development of GNRs in which carbon atoms have been selectively replaced by heteroatoms at predetermined positions.[137-140] The most extensively studied class of GNRs subjected to doping investigations is the chevron GNR.[141-144] This is achieved by substitution of the C–H group composing the armchair edges of the ribbon with sp^2 hybridized nitrogen atoms. A typical example of molecular precursors used for the preparation of N-doped chevron GNRs is depicted in Figure X.12A.

Surface-mediated polymerization of bis-pyrimidine unit **27** followed by cyclodehydrogenation to yield N-doped GNRs was reported both by the group of *Sinitskii* and by the group of *Fasel*.[141, 142, 144] Through the combined use of different microscopy techniques (*e.g.* STM, HR-TEM and optical microscopy), the group of *Sinitskii* was able to show that substitutional doping with nitrogen atoms was able to trigger a self-assembly process both on metallic surfaces and in the solid state. Whereas undoped chevron GNRs showed no detectable secondary arrangements, nitrogen doped GNRs formed by thermal annealing of **27** on Au(111), showed the formation of 2-D assemblies in which isolated GNRs arranged edge to edge (Figure X.12B). Such an arrangement could be potentially explained by the formation of multiple hydrogen bond interactions between the nitrogen and the C–H groups of adjacent GNRs. Despite the many examples of doped chevron GNRs, the periodic incorporation of heteroatoms into straight armchair edges GNRs remains a considerable challenge. In a very recent work, *Fischer* and *Crommie* and independently the group of *Kawai* published the first example of straight N=7 **AGNRs** incorporating Boron atoms.[145, 146] Submitting molecular precursor **28** to the surface-mediated polymerization/cyclodehydrogenation sequence (Figure X.12C-D) produced **7-AGNRs** featuring a regioregular pattern of boron atoms along the central backbone of the ribbon. LT-STM (13K) imaging of a Au(111) sample on which **28** was firstly polymerized at 220°C and then fully cyclized by further thermal treatment at 330°C, showed the formation of GNRs featuring a characteristic longitudinal stripe pattern with a periodicity corresponding to the distance between the expected position of the boron atoms. First principles calculations, aimed to better understand the effect of the boron doping on the electronic structure of the **7-AGNR**, revealed the presence of a new acceptor band (0.8 eV above the VB maximum), which shows a significant contribution (10%) from the boron atom and an energy comprised in the gap of the undoped **7-AGNR**. As a consequence of the doping, the theoretically predicted band-gap (0.8 eV) of the boron doped **7-AGNR** becomes considerably smaller than the one of the undoped **7-AGNRs** (~2.1eV) calculated with the same method. Experimental confirmation of this predicted electronic structure was obtained through *dI/dV* mapping, which showed the existence of LDOS along the backbone of the ribbon at an operative voltage V_s= 1.0 V corresponding to the Conduction Band. Such results, which strongly differ from the mapping of undoped **7-AGNR**, provide additional evidence that the substitution of carbon atoms with trigonal planar boron atoms is introducing a new band in the DOS of the **7-AGNR** modifying drastically its electronic structure.
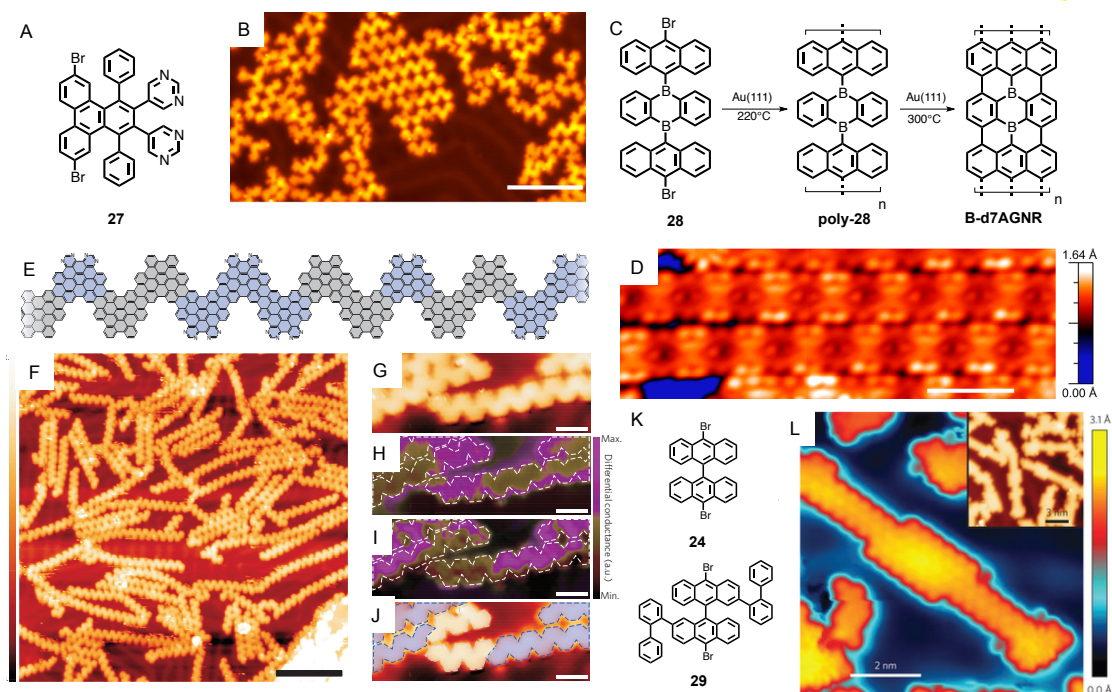
Figure X.12. Molecular structure (A) of bispyrimidine monomer **27**. LT-STM images (B) of nitrogen doped chevron GNRs obtained from **27** on Au(111) (Reproduced from ref. 142 with permission from the American Chemical Society). Schematic representations (C) of the surface mediated synthesis of Boron doped **7-AGNR** starting from precursor **28** and its LT-STM topography (D) (Reproduced from ref. 145 with permission from the American Chemical Society). Structural representation (E) of a chevron nanoribbon combining doped (blue) and undoped (grey) segments, and a large scale STM image (F) of the GNR heterostructures on Au(111). Smaller scale (G) STM images of a GNR heterojunction and the corresponding differential conductance dI/dV maps taken at bias voltages of U = –0.35 V (H) and –1.65 V (I) respectively, showing two chemically different ribbon segments (J) which are highlighted with blue colour (scale bar 2 nm) (Reproduced from ref. 144 with permission from The Nature Publishing Group). Molecular structures (K) of precursors **25** and **29**, used for the construction of 7-13 GNR hetereojunction. LT-STM topographic image (L) of a 7–13 GNR heterojunction (inset: larger-scale showing the sample composition and multiple GNR heterojunctions) (Reproduced from ref. 147 with permission from The Nature Publishing Group).

A further evolution on the construction of GNR based architecture using both pristine and nitrogen doped GNRs was performed by the groups of *Mullen* and *Fasel*.[144] By co-deposition of tetraphenylene unit **26** and the nitrogen doped monomer **27** on an Au(111) surface and subsequent thermal polymerization/cyclodehydrogenation synthesis, the authors were able to grow GNR heterostructures composed of both pristine hydrocarbon precursors and their nitrogen-substituted equivalent. LT-STM imaging and *dI/dV* mapping of the resulting architecture, showed the formation of GNRs composed of a statistical mixture of doped and undoped segments (Figure X.12E-J). A combination of DFT calculations and *dI/dV* mapping of this GNR heterostructure showed the presence of a band shift of 0.5 eV at the interface between the doped and undoped section of the chevron GNRs and an electric field of 2×10^8 V m^{-1}. In particular, DFT computations showed a significant downshift of 0.45 eV and 0.55 eV for the valence

band and conduction band as passing from the undoped to the nitrogen doped section of the GNR, indicating a possible staggered band-gap configuration.

Another type of hybrid architecture based on GNR recently demonstrated by *Fischer* and *Crommie* groups exploits the different electronic properties of armchair GNR featuring different width.[147] Accordingly with their predicted electronic behaviour, armchair GNRs can be classified into three main groups, N = 3p, N = 3p + 1 and N = 3p + 2, where p is an integer and N is the number of carbon atoms across the GNR width.[118, 120, 148] All families of GNRs are predicted to have a pronounced bandgap which scales inversely with the ribbon width, with the N = 3p + 2 having the smallest predicted bandgaps.[149] Due to the great variation in band-gaps between GNRs of different families, the construction of hybrid GNR architectures featuring sections of different widths results is be an extremely promising method to fabricate semiconductor heterostructures that could be used to perform processes such as resonant tunnelling and solar energy conversion.

GNR based hetero junctions were fabricated by combining two different types of the molecular building blocks: bisanthracene derivatives **25** and **29** (Figure X.12K). These molecules, which are precursors for N=7 and N=13 armchair GNRs, were sublimed onto a Au(111) surface and submitted to surface mediated polymerization at 420 °K and to a subsequent cyclodehydrogenation step at 640 °K. A typical architecture obtained through this method is depicted in Figure X.12L. As expected, LT-STM images show 1D graphitic structures composed of sections featuring different widths, in which the narrower segments (1.3 ± 0.1 nm in width) are made of covalently bonded monomers of **25** (N = 7) and the wider segments (1.9 ± 0.2 nm in width) consist of bonded monomers of **29** (N = 13). Interestingly, subnanometer scale investigation of the electronic properties of these heterojunctions by STS and *dI/dV* mapping, in combination with DFT simulation were able to show that the band alignment in the 7/13-GNR heterojunction can be considered very similar to the one that conventionally is associated with type I semiconductor junction. Such findings could potentially pave the way to the possible application of this type of junction for the construction of graphene-based quantum dots and bandgap-modulated semiconductor junctions smaller than the ones obtainable through lithographic methods.

Very recently also more complex GNR topologies have been developed through surface mediated synthesis. The group of *Mullen* has reported the fabrication of cove type-GNRs through surface mediated synthesis. In this case the formation of cove-edged GNR was obtain through surface mediated polymerization/cyclodehydrogenation of the dibrominated chrysene derivative **30** on Au(111) at 160°C and 360°C respectively (Figure X.13).[150] Interestingly, when similar types of targets were attempted using conventional solution synthesis (*Ullmann* type polymerization and (FeCl$_3$) or DDQ/trifluoromethanesulfonic acid as the Lewis acid/oxidant) only very short ribbons were obtained (up to octamers). Such low degree of polymerization can be rationalized taking in consideration the very high steric hindrance during the coupling

reaction between the C–H groups in the chrysene "bay-positions" of **30**. On the other hand, using a surface mediated approach it was possible to increase the length of the GNRs up to 20 nm. Indeed, monomers on surfaces are confined in just two dimensions (as opposite to the three dimension of the solution environment), which could potentially increase the statistical probability of monomers reacting with each other to form longer oligomers. In addition, as seen in previous examples, also the Au(111) surface could potentially play a role in term of catalytic activity necessary to drive the polymerization and cyclodehydrogenation reaction to completion, favouring in this way the formation of longer oligomeric structure.
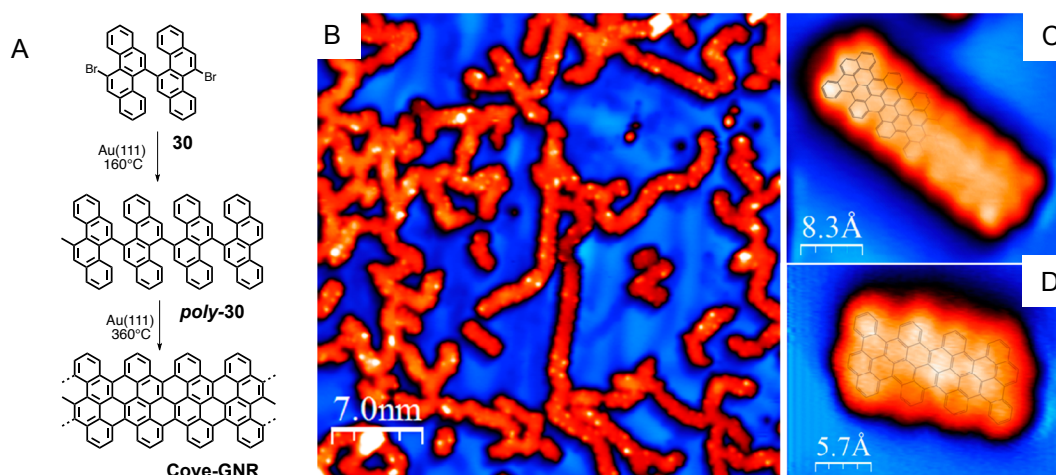

Figure X.13. Schematic representations (A) of the surface mediated synthesis of cove edge GNRs starting from chrysene derivative **30**. Long range (B) and high-resolution (C-D) STM images of cove edged GNRs as obtained after cyclodehydrogenation of poly-chrisene oligomers (a schematic model is overlayed for clarity) (Reproduced from ref. 150 with permission from the American Chemical Society).

Very characteristic of this new type of ribbon is the fact that, as highlighted by both X-Ray crystal structure of the dimers obtained in solution and DFT simulation, they do not possess a completely planar structure. Indeed due to steric repulsion the benzenoid rings in the cove region of the GNR adopt alternating "up-down" conformation, which can deviate from planarity the GNR carbon framework.

X.4 Conclusions

The most important advancements over the last decades regarding structural investigations and reactivity of aromatic molecules on crystalline surfaces have been discussed in this chapter. The invention and the continuing development of Scanning Probe Microscopy techniques allows for the investigation of isolated aromatic molecules adsorbed onto inorganic surfaces with a submolecular level of resolution. Techniques

such as STM, STHM, nc-AFM and KPFM are extremely valuable for understanding and elucidating the structural and electronic properties of planar aromatic molecules adsorbed on surfaces.

The first section of this chapter introduces the reader to the basic principles behind these types of scanning probe techniques and describes their use in the investigations of different aromatic molecules. Applications of different probe techniques for the investigation of important properties such as atomic interconnectivity, bond-order evaluation and sub-molecular charge distribution have been discussed.

In the second part of the chapter, reactivity of aromatic molecules on metallic surfaces is discussed presenting the principal class of reactions that have been developed. The construction of polymeric systems, 2-D networks, extended polyaromatic hydrocarbons and graphene derivatives (*i.e.* Graphene Nanoribbons) starting from aromatic molecular precursors have been detailed. Particular emphasis has been placed on the role of the surface during the different reactions and the differences between the reactivity that the same molecules can have if submitted to analogous "solution-based" reactions. Following these many examples, it can be concluded that metal surface mediated synthesis can be efficiently employed to construct highly conjugated organic architectures, which can be investigated with high accuracy by SPM techniques.

X.5 Bibliography

1. J. M. MacLeod and F. Rosei, *Small*, 2014, **10**, 1038-1049.
2. J. W. Colson, A. R. Woll, A. Mukherjee, M. P. Levendorf, E. L. Spitler, V. B. Shields, M. G. Spencer, J. Park and W. R. Dichtel, *Science*, 2011, **332**, 228-231.
3. S. A. DiBenedetto, A. Facchetti, M. A. Ratner and T. J. Marks, *Adv. Mater.*, 2009, **21**, 1407-1433.
4. E. Goiri, P. Borghetti, A. El-Sayed, J. E. Ortega and D. G. de Oteyza, *Adv. Mater.*, 2016, **28**, 1340-1368.
5. N. Katsonis, M. Lubomska, M. M. Pollard, B. L. Feringa and P. Rudolf, *Prog. Surf. Sci.*, 2007, **82**, 407-434.
6. J. Mendez, M. F. Lopez and J. A. Martin-Gago, *Chem. Soc. Rev.*, 2011, **40**, 4578-4590.
7. H. Klauk, *Chem. Soc. Rev.*, 2010, **39**, 2643-2666.
8. J. K. Gimzewski and C. Joachim, *Science*, 1999, **283**, 1683-1688.
9. P. Sundberg and M. Karppinen, *Beilstein J. Nanotechnol.*, 2014, **5**, 1104-1136.
10. T. Bjornholm, T. Hassenkam and N. Reitzel, *J. Mater. Chem.*, 1999, **9**, 1975-1990.
11. S. R. Forrest, *Chem. Rev.*, 1997, **97**, 1793-1896.
12. D. B. Hall, P. Underhill and J. M. Torkelson, *Polym. Eng. Sci.*, 1998, **38**, 2039-2045.
13. H. Alves, A. S. Molinari, H. Xie and A. F. Morpurgo, *Nat. Mater.*, 2008, **7**, 574-580.
14. K. Norbert, *J. Phys.: Condens. Matter*, 2008, **20**, 184008.

15. G. Vasseur, Y. Fagot-Revurat, M. Sicot, B. Kierren, L. Moreau, D. Malterre, L. Cardenas, G. Galeotti, J. Lipton-Duffin, F. Rosei, M. Di Giovannantonio, G. Contini, P. Le Fevre, F. Bertran, L. Liang, V. Meunier and D. F. Perepichka, *Nat. Commun.*, 2016, **7**.

16. K. Müller, A. P. Seitsonen, T. Brugger, J. Westover, T. Greber, T. Jung and A. Kara, *J. Phys. Chem. C*, 2012, **116**, 23465-23471.

17. L. Schulz, L. Nuccio, M. Willis, P. Desai, P. Shakya, T. Kreouzis, V. K. Malik, C. Bernhard, F. L. Pratt, N. A. Morley, A. Suter, G. J. Nieuwenhuys, T. Prokscha, E. Morenzoni, W. P. Gillin and A. J. Drew, *Nat. Mater.*, 2011, **10**, 39-44.

18. J. H. Burroughes, D. D. C. Bradley, A. R. Brown, R. N. Marks, K. Mackay, R. H. Friend, P. L. Burns and A. B. Holmes, *Nature*, 1990, **347**, 539-541.

19. K. T. Kamtekar, A. P. Monkman and M. R. Bryce, *Adv. Mater.*, 2010, **22**, 572-582.

20. A. Pogantsch, S. Rentenberger, G. Langer, J. Keplinger, W. Kern and E. Zojer, *Adv. Funct. Mater.*, 2005, **15**, 403-409.

21. L. Zhai, S. I. Khondaker, J. Thomas, C. Shen and M. McInnis, *Nano Today*, 2014, **9**, 705-721.

22. T. W. Kelley, P. F. Baude, C. Gerlach, D. E. Ender, D. Muyres, M. A. Haase, D. E. Vogel and S. D. Theiss, *Chem. Mater.*, 2004, **16**, 4413-4422.

23. C. Reese, M. Roberts, M.-m. Ling and Z. Bao, *Mater. Today*, 2004, **7**, 20-27.

24. S. Z. Bisri, C. Piliego, J. Gao and M. A. Loi, *Adv. Mater.*, 2014, **26**, 1176-1199.

25. K. Oura, V. G. Lifshits, A. A. Saranin, A. V. Zotov and M. Katayama (2003). *Surface Science, An Introduction.* Berlin: Springer.

26. G. R. Binnig and H. Rohrer, *IBM Journal of Research and Development* (1986). **30** 355–369.

27. C. Julian Chen, *Introduction to Scanning Tunneling Microscopy: Second Edition*, Oxford University Press.

28. A. Della Pia and G. Costantini, in *Encyclopedia of Nanotechnology*, ed. B. Bhushan, Springer Netherlands, 2012, pp. 2301-2313.

29. S. Kano, T. Tada and Y. Majima, *Chem. Soc. Rev.*, 2015, **44**, 970-987.

30. M. S. J. Marshall and M. R. Castell, *Chem. Soc. Rev.*, 2014, **43**, 2226-2239.

31. H. Arakawa, K. Umemura and A. Ikai, *Nature*, 1992, **358**, 171-173.

32. P. G. Arscott and V. A. Bloomfield, *Trends Biotechnol.*, 1990, **8**, 151-156.

33. L. Gross, *Nat. Chem.*, 2011, **3**, 273-278.

34. R. Temirov, S. Soubatch, O. Neucheva, A. C. Lassise and F. S. Tautz, *New J. Phys.*, 2008, **10**, 053012.

35. C. Weiss, C. Wagner, R. Temirov and F. S. Tautz, *J. Am. Chem. Soc.*, 2010, **132**, 11864-11865.

36. S. Morita, F. J. Giessibl and R. Wiesendanger, *Noncontact Atomic Force Microscopy*, Springer, 2009.

37. F. J. Giessibl, *Appl. Phys. Lett.*, 1998, **73**, 3956-3958.

38. L. Gross, F. Mohn, N. Moll, P. Liljeroth and G. Meyer, *Science*, 2009, **325**, 1110-1114.

39. L. Gross, B. Schuler, F. Mohn, N. Moll, J. Repp and G. Meyer, in *Noncontact Atomic Force Microscopy*, ed. Springer, 2015, vol. 3, pp. 223-246.

40. N. Moll, B. Schuler, S. Kawai, F. Xu, L. Peng, A. Orita, J. Otera, A. Curioni, M. Neu, J. Repp, G. Meyer and L. Gross, *Nano Lett.*, 2014, **14**, 6127-6131.

41. L. Gross, F. Mohn, N. Moll, B. Schuler, A. Criado, E. Guitián, D. Peña, A. Gourdon and G. Meyer, *Science*, 2012, **337**, 1326-1329.

42. W. I. F. David, R. M. Ibberson, J. C. Matthewman, K. Prassides, T. J. S. Dennis, J. P. Hare, H. W. Kroto, R. Taylor and D. R. M. Walton, *Nature*, 1991, **353**, 147-149.

43. K. Hedberg, L. Hedberg, D. S. Bethune, C. A. Brown, H. C. Dorn, R. D. Johnson And M. De Vries, *Science*, 1991, **254**, 410-412.

44. F. Mohn, L. Gross, N. Moll and G. Meyer, *Nat. Nanotehnol.*, 2012, **7**, 227-231.

45. B. Schuler, G. Meyer, D. Peña, O. C. Mullins and L. Gross, *J. Am. Chem. Soc.*, 2015, **137**, 9870-9876.

46. Q. Fan, J. M. Gottfried and J. Zhu, *Acc. Chem. Res.*, 2015, **48**, 2484-2494.

47. G. Franc and A. Gourdon, *Phys. Chem. Chem. Phys.*, 2011, **13**, 14283-14292.

48. A. Gourdon, *Angew. Chem. Int. Ed.*, 2008, **47**, 6950-6953.

49. X. Zhang, Q. Zeng and C. Wang, *Nanoscale*, 2013, **5**, 8269-8287.

50. F. Klappenberger, Y.-Q. Zhang, J. Björk, S. Klyatskaya, M. Ruben and J. V. Barth, *Acc. Chem. Res.*, 2015, **48**, 2140-2150.

51. B. Cirera, Y.-Q. Zhang, J. Björk, S. Klyatskaya, Z. Chen, M. Ruben, J. V. Barth and F. Klappenberger, *Nano Lett.*, 2014, **14**, 1891-1897.

52. A. Riss, S. Wickenburg, P. Gorman, L. Z. Tan, H.-Z. Tsai, D. G. de Oteyza, Y.-C. Chen, A. J. Bradley, M. M. Ugeda, G. Etkin, S. G. Louie, F. R. Fischer and M. F. Crommie, *Nano Lett.*, 2014, **14**, 2251-2255.

53. R. Bates, in *Organic Synthesis Using Transition Metals*, John Wiley & Sons, Ltd, 2012, pp. i-xv.

54. J. F. Hartwig, *Organotransition Metal Chemistry, from Bonding to Catalysis*, 2010, University Science Books: New York.

55. Y.-Q. Zhang, N. Kepčija, M. Kleinschrodt, K. Diller, S. Fischer, A. C. Papageorgiou, F. Allegretti, J. Björk, S. Klyatskaya, F. Klappenberger, M. Ruben and J. V. Barth, *Nat. Commun.*, 2012, **3**, 1286.

56. J. Liu, P. Ruffieux, X. Feng, K. Mullen and R. Fasel, *Chem. Commun.*, 2014, **50**, 11200-11203.

57.   F. Bebensee, C. Bombis, S.-R. Vadapoo, J. R. Cramer, F. Besenbacher, K. V. Gothelf and T. R. Linderoth, *J. Am. Chem. Soc.*, 2013, **135**, 2136-2139.

58.   O. Díaz Arado, H. Mönig, H. Wagner, J.-H. Franke, G. Langewisch, P. A. Held, A. Studer and H. Fuchs, *ACS Nano*, 2013, **7**, 8509-8515.

59.   J. Eichhorn, D. Nieckarz, O. Ochs, D. Samanta, M. Schmittel, P. J. Szabelski and M. Lackinger, *ACS Nano*, 2014, **8**, 7880-7889.

60.   L. Grill, M. Dyer, L. Lafferentz, M. Persson, M. V. Peters and S. Hecht, *Nat. Nanotechnol.*, 2007, **2**, 687-691.

61.   M. Bieri, M.-T. Nguyen, O. Gröning, J. Cai, M. Treier, K. Aït-Mansour, P. Ruffieux, C. A. Pignedoli, D. Passerone, M. Kastler, K. Müllen and R. Fasel, *J. Am. Chem. Soc.*, 2010, **132**, 16669-16676.

62.   G. Eder, E. F. Smith, I. Cebula, W. M. Heckl, P. H. Beton and M. Lackinger, *ACS Nano*, 2013, **7**, 3014-3021.

63.   L. Ferrighi, I. Píš, T. H. Nguyen, M. Cattelan, S. Nappini, A. Basagni, M. Parravicini, A. Papagni, F. Sedona, E. Magnano, F. Bondino, C. Di Valentin and S. Agnoli, *Chem. Eur. J.*, 2015, **21**, 5826-5835.

64.   D. R. Lide, *Handbook of Chemistry and Physics 90th edn* (CRC Press, 2010). .

65.   L. Lafferentz, V. Eberhardt, C. Dri, C. Africh, G. Comelli, F. Esch, S. Hecht and L. Grill, *Nat. Chem.*, 2012, **4**, 215-220.

66.   T. Dienel, J. Gómez-Díaz, A. P. Seitsonen, R. Widmer, M. Iannuzzi, K. Radican, H. Sachdev, K. Müllen, J. Hutter and O. Gröning, *ACS Nano*, 2014, **8**, 6571-6579.

67.   Y. Jin, C. Yu, R. J. Denman and W. Zhang, *Chem. Soc. Rev.*, 2013, **42**, 6634-6654.

68.   S. J. Rowan, S. J. Cantrill, G. R. L. Cousins, J. K. M. Sanders and J. F. Stoddart, *Angew. Chem. Int. Ed.*, 2002, **41**, 898-952.

69.   A. Ciesielski, M. El Garah, S. Haar, P. Kovaříček, J.-M. Lehn and P. Samorì, *Nat. Chem.*, 2014, **6**, 1017-1023.

70.   J. Plas, D. Waghray, J. Adisoejoso, O. Ivasenko, W. Dehaen and S. De Feyter, *Chem. Commun.*, 2015, **51**, 16338-16341.

71.   X.-H. Liu, Y.-P. Mo, J.-Y. Yue, Q.-N. Zheng, H.-J. Yan, D. Wang and L.-J. Wan, *Small*, 2014, **10**, 4934-4939.

72.   L. Xu, X. Zhou, Y. Yu, W. Q. Tian, J. Ma and S. Lei, *ACS Nano*, 2013, **7**, 8066-8073.

73.   Y. Yu, J. Sun and S. Lei, *J. Phys. Chem. C*, 2015, **119**, 16777-16784.

74.   C.-Z. Guan, D. Wang and L.-J. Wan, *Chem. Commun.*, 2012, **48**, 2943-2945.

75.   S. Kandambeth, A. Mallick, B. Lukose, M. V. Mane, T. Heine and R. Banerjee, *J. Am. Chem. Soc.*, 2012, **134**, 19524-19527.

76.   S. Clair, M. Abel and L. Porte, *Chem. Commun.*, 2014, **50**, 9627-9635.

77.   R. Tanoue, R. Higuchi, N. Enoki, Y. Miyasato, S. Uemura, N. Kimizuka, A. Z. Stieg, J. K. Gimzewski and M. Kunitake, *ACS Nano*, 2011, **5**, 3923-3929.

78.   N. A. A. Zwaneveld, R. Pawlak, M. Abel, D. Catalin, D. Gigmes, D. Bertin and L. Porte, *J. Am. Chem. Soc.*, 2008, **130**, 6678-6679.

79.   J. F. Dienstmaier, D. D. Medina, M. Dogru, P. Knochel, T. Bein, W. M. Heckl and M. Lackinger, *ACS Nano*, 2012, **6**, 7234-7242.

80.   M. Grzybowski, K. Skonieczny, H. Butenschön and D. T. Gryko, *Angew. Chem. Int. Ed.* 2013, **52**, 9900-9930.

81.   B. T. King, J. Kroulík, C. R. Robertson, P. Rempala, C. L. Hilton, J. D. Korinek and L. M. Gortari, *J. Org. Chem.*, 2007, **72**, 2279-2288.

82.   P. Kovacic and M. B. Jones, *Chem. Rev.*, 1987, **87**, 357-379.

83.   A. T. Balaban, C. D. Nenitzescu and G. A. Olah, *Friedel-Crafts and Related Reactions,* Interscience Ed. New York , 1964, vol. 2, p. 979.

84.   X. Dou, X. Yang, G. J. Bodwell, M. Wagner, V. Enkelmann and K. Müllen, *Org. Lett.*, 2007, **9**, 2485-2488.

85.   S. L. Skraba-Joiner, E. C. McLaughlin, A. Ajaz, R. Thamatam and R. P. Johnson, *J. Org. Chem.*, 2015, **80**, 9578-9583.

86.   J. L. Ormsby, T. D. Black, C. L. Hilton, Bharat and B. T. King, *Tetrahedron*, 2008, **64**, 11370-11378.

87.   A. Ajaz, E. C. McLaughlin, S. L. Skraba, R. Thamatam and R. P. Johnson, *J. Org. Chem.*, 2012, **77**, 9487-9495.

88.   M. Treier, C. A. Pignedoli, T. Laino, R. Rieger, K. Müllen, D. Passerone and R. Fasel, *Nat. Chem.*, 2011, **3**, 61-67.

89.   C. Rogers, C. Chen, Z. Pedramrazi, A. A. Omrani, H.-Z. Tsai, H. S. Jung, S. Lin, M. F. Crommie and F. R. Fischer, *Angew. Chem. Int. Ed.*, 2015, **54**, 15143-15146.

90.   L. Zöphel, R. Berger, P. Gao, V. Enkelmann, M. Baumgarten, M. Wagner and K. Müllen, *Chem. Eur. J.*, 2013, **19**, 17821-17826.

91.   X. Zhang, J. Li, H. Qu, C. Chi and J. Wu, *Org. Lett.*, 2010, **12**, 3946-3949.

92.   Q. Ye and C. Chi, *Chem. Mater.*, 2014, **26**, 4046-4056.

93.   Z. Sun, Q. Ye, C. Chi and J. Wu, *Chem. Soc. Rev.*, 2012, **41**, 7857-7889.

94.   G. Otero, G. Biddau, C. Sanchez-Sanchez, R. Caillard, M. F. Lopez, C. Rogero, F. J. Palomares, N. Cabello, M. A. Basanta, J. Ortega, J. Mendez, A. M. Echavarren, R. Perez, B. Gomez-Lor and J. A. Martin-Gago, *Nature*, 2008, **454**, 865-868.

95. A. L. Pinardi, G. Otero-Irurueta, I. Palacio, J. I. Martinez, C. Sanchez-Sanchez, M. Tello, C. Rogero, A. Cossaro, A. Preobrajenski, B. Gómez-Lor, A. Jancarik, I. G. Stará, I. Starý, M. F. Lopez, J. Méndez and J. A. Martin-Gago, *ACS Nano*, 2013, **7**, 3676-3684.

96. Y.-F. Zhang, N. Zhu and T. Komeda, *J. Phys. Chem. C*, 2007, **111**, 16946-16950.

97. U. Schlickum, R. Decker, F. Klappenberger, G. Zoppellaro, S. Klyatskaya, W. Auwärter, S. Neppl, K. Kern, H. Brune, M. Ruben and J. V. Barth, *J. Am. Chem. Soc.*, 2008, **130**, 11778-11782.

98. U. Schlickum, R. Decker, F. Klappenberger, G. Zoppellaro, S. Klyatskaya, M. Ruben, I. Silanes, A. Arnau, K. Kern, H. Brune and J. V. Barth, *Nano Lett.*, 2007, **7**, 3813-3817.

99. C. S. Kley, J. Čechal, T. Kumagai, F. Schramm, M. Ruben, S. Stepanow and K. Kern, *J. Am. Chem. Soc.*, 2012, **134**, 6072-6075.

100. NOTE: An assymetric configuration with monodentates axyal ligands was also observed in some cases.

101. W. Auwarter, D. Ecija, F. Klappenberger and J. V. Barth, *Nat. Chem.*, 2015, **7**, 105-120.

102. T. A. Pham, F. Song, M. N. Alberti, M.-T. Nguyen, N. Trapp, C. Thilgen, F. Diederich and M. Stohr, *Chem. Commun.*, 2015, **51**, 14473-14476.

103. J. I. Urgel, D. Ecija, W. Auwärter, D. Stassen, D. Bonifazi and J. V. Barth, *Angew. Chem. Int. Ed.*, 2015, **54**, 6163-6167.

104. J. I. Urgel, M. Schwarz, M. Garnica, D. Stassen, D. Bonifazi, D. Ecija, J. V. Barth and W. Auwärter, *J. Am. Chem. Soc.*, 2015, **137**, 2420-2423.

105. M. El Garah, N. Marets, M. Mauro, A. Aliprandi, S. Bonacchi, L. De Cola, A. Ciesielski, V. Bulach, M. W. Hosseini and P. Samorì, *J. Am. Chem. Soc.*, 2015, **137**, 8450-8459.

106. Y. Li, J. Xiao, T. E. Shubina, M. Chen, Z. Shi, M. Schmid, H.-P. Steinrück, J. M. Gottfried and N. Lin, *J. Am. Chem. Soc.*, 2012, **134**, 6401-6408.

107. D. Heim, D. Écija, K. Seufert, W. Auwärter, C. Aurisicchio, C. Fabbro, D. Bonifazi and J. V. Barth, *J. Am. Chem. Soc.*, 2010, **132**, 6783-6790.

108. S. Haq, F. Hanke, M. S. Dyer, M. Persson, P. Iavicoli, D. B. Amabilino and R. Raval, *J. Am. Chem. Soc.*, 2011, **133**, 12031-12039.

109. H. Marbach, *Acc. Chem. Res.*, 2015, **48**, 2649-2658.

110. J. Mielke, F. Hanke, M. V. Peters, S. Hecht, M. Persson and L. Grill, *J. Am. Chem. Soc.*, 2015, **137**, 1844-1849.

111. K. S. Novoselov, A. K. Geim, S. V. Morozov, D. Jiang, Y. Zhang, S. V. Dubonos, I. V. Grigorieva and A. A. Firsov, *Science*, 2004, **306**, 666-669.

112. K. S. Novoselov, V. I. Falko, L. Colombo, P. R. Gellert, M. G. Schwab and K. Kim, *Nature*, 2012, **490**, 192-200.

113. A. H. Castro Neto, F. Guinea, N. M. R. Peres, K. S. Novoselov and A. K. Geim, *Rev. Mod. Phys.*, 2009, **81**, 109-162.

114. W. Han, R. K. Kawakami, M. Gmitra and J. Fabian, *Nat. Nanotchnol.*, 2014, **9**, 794-807.

115. A. C. Ferrari, F. Bonaccorso, V. Fal'ko, K. S. Novoselov, S. Roche, P. Boggild, S. Borini, F. H. L. Koppens, V. Palermo, N. Pugno, J. A. Garrido, R. Sordan, A. Bianco, L. Ballerini, M. Prato, E. Lidorikis, J. Kivioja, C. Marinelli, T. Ryhanen, A. Morpurgo, J. N. Coleman, V. Nicolosi, L. Colombo, A. Fert, M. Garcia-Hernandez, A. Bachtold, G. F. Schneider, F. Guinea, C. Dekker, M. Barbone, Z. Sun, C. Galiotis, A. N. Grigorenko, G. Konstantatos, A. Kis, M. Katsnelson, L. Vandersypen, A. Loiseau, V. Morandi, D. Neumaier, E. Treossi, V. Pellegrini, M. Polini, A. Tredicucci, G. M. Williams, B. Hee Hong, J.-H. Ahn, J. Min Kim, H. Zirath, B. J. van Wees, H. van der Zant, L. Occhipinti, A. Di Matteo, I. A. Kinloch, T. Seyller, E. Quesnel, X. Feng, K. Teo, N. Rupesinghe, P. Hakonen, S. R. T. Neil, Q. Tannock, T. Lofwander and J. Kinaret, *Nanoscale*, 2015, **7**, 4598-4810.

116. A. V. Rozhkov, S. Savel'ev and F. Nori, *Phys. Rev. B*, 2009, **79**, 125420.

117. O. V. Yazyev, *Acc. Chem. Res.*, 2013, **46**, 2319-2328.

118. L. Yang, C.-H. Park, Y.-W. Son, M. L. Cohen and S. G. Louie, *Phys. Rev. Lett.*, 2007, **99**, 186801.

119. C.-S. Wu and J.-D. Chai, *J. Chem. Theory Comput.*, 2015, **11**, 2003-2011.

120. K. Nakada, M. Fujita, G. Dresselhaus and M. S. Dresselhaus, *Phys. Rev. B*, 1996, **54**, 17954-17961.

121. Y.-W. Son, M. L. Cohen and S. G. Louie, *Phys. Rev. Lett.*, 2006, **97**, 216803.

122. V. Barone, O. Hod and G. E. Scuseria, *Nano Lett.*, 2006, **6**, 2748-2754.

123. M. Fujita, K. Wakabayashi, K. Nakada and K. Kusakabe, *J. Phys. Soc. Jpn.*, 1996, **65**, 1920-1923.

124. W. Huang, J.-S. Wang and G. Liang, *Phys. Rev. B*, 2011, **84**, 045410.

125. Y. Chen, T. Jayasekera, A. Calzolari, K. W. Kim and M. B. Nardelli, *J. Phys.: Condens. Matter*, 2010, **22**, 372202.

126. S. Wang and J. Wang, *J. Phys. Chem. C*, 2012, **116**, 10193-10197.

127. J. Cai, P. Ruffieux, R. Jaafar, M. Bieri, T. Braun, S. Blankenburg, M. Muoth, A. P. Seitsonen, M. Saleh, X. Feng, K. Mullen and R. Fasel, *Nature*, 2010, **466**, 470-473.

128. P. Han, K. Akagi, F. Federici Canova, R. Shimizu, H. Oguchi, S. Shiraki, P. S. Weiss, N. Asao and T. Hitosugi, *ACS Nano*, 2015, **9**, 12035-12044.

129. K. A. Simonov, N. A. Vinogradov, A. S. Vinogradov, A. V. Generalov, E. M. Zagrebina, G. I. Svirskiy, A. A. Cafolla, T. Carpy, J. P. Cunniffe, T. Taketsugu, A. Lyalin, N. Mårtensson and A. B. Preobrajenski, *ACS Nano*, 2015, **9**, 8997-9011.

130. L. Massimi, O. Ourdjini, L. Lafferentz, M. Koch, L. Grill, E. Cavaliere, L. Gavioli, C. Cardoso, D. Prezzi, E. Molinari, A. Ferretti, C. Mariani and M. G. Betti, *J. Phys. Chem. C*, 2015, **119**, 2427-2437.

131. P. Han, K. Akagi, F. Federici Canova, H. Mutoh, S. Shiraki, K. Iwaya, P. S. Weiss, N. Asao and T. Hitosugi, *ACS Nano*, 2014, **8**, 9181-9187.

132. A. Kimouche, M. M. Ervasti, R. Drost, S. Halonen, A. Harju, P. M. Joensuu, J. Sainio and P. Liljeroth, *Nat. Commun.*, 2015, **6**.

133. Y.-C. Chen, D. G. de Oteyza, Z. Pedramrazi, C. Chen, F. R. Fischer and M. F. Crommie, *ACS Nano*, 2013, **7**, 6123-6128.

134. P. Ruffieux, J. Cai, N. C. Plumb, L. Patthey, D. Prezzi, A. Ferretti, E. Molinari, X. Feng, K. Müllen, C. A. Pignedoli and R. Fasel, *ACS Nano*, 2012, **6**, 6930-6935.

135. J. van der Lit, M. P. Boneschanscher, D. Vanmaekelbergh, M. Ijäs, A. Uppstu, M. Ervasti, A. Harju, P. Liljeroth and I. Swart, *Nat. Commun.*, 2013, **4**.

136. J. Björk, S. Stafström and F. Hanke, *J. Am. Chem. Soc.*, 2011, **133**, 14884-14887.

137. Y. Li, Z. Zhou, P. Shen and Z. Chen, *ACS Nano*, 2009, **3**, 1952-1958.

138. H. Kim, K. Lee, S. I. Woo and Y. Jung, *Phys. Chem. Chem. Phys.*, 2011, **13**, 17505-17510.

139. A. E. Torres and S. Fomine, *Phys. Chem. Chem. Phys.*, 2015, **17**, 10608-10614.

140. D. J. Dibble, Y. S. Park, A. Mazaheripour, M. J. Umerani, J. W. Ziller and A. A. Gorodetsky, *Angew. Chem. Int. Ed.*, 2015, **54**, 5883-5887.

141. T. H. Vo, M. Shekhirev, D. A. Kunkel, F. Orange, M. J. F. Guinel, A. Enders and A. Sinitskii, *Chem. Commun.*, 2014, **50**, 4172-4174.

142. T. H. Vo, U. G. E. Perera, M. Shekhirev, M. Mehdi Pour, D. A. Kunkel, H. Lu, A. Gruverman, E. Sutter, M. Cotlet, D. Nykypanchuk, P. Zahl, A. Enders, A. Sinitskii and P. Sutter, *Nano Lett.*, 2015, **15**, 5770-5777.

143. C. Bronner, S. Stremlau, M. Gille, F. Brauße, A. Haase, S. Hecht and P. Tegeder, *Angew. Chem. Int. Ed.*, 2013, **52**, 4422-4425.

144. J. Cai, C. A. Pignedoli, L. Talirz, P. Ruffieux, H. Söde, L. Liang, V. Meunier, R. Berger, R. Li, X. Feng, K. Müllen and R. Fasel, *Nat. Nanotechnol.*, 2014, **9**, 896-900.

145. R. R. Cloke, T. Marangoni, G. D. Nguyen, T. Joshi, D. J. Rizzo, C. Bronner, T. Cao, S. G. Louie, M. F. Crommie and F. R. Fischer, *J. Am. Chem. Soc.*, 2015, **137**, 8872-8875.

146. S. Kawai, S. Saito, S. Osumi, S. Yamaguchi, A. S. Foster, P. Spijker and E. Meyer, *Nat. Commun.*, 2015, **6**.

147. Y.-C. Chen, T. Cao, C. Chen, Z. Pedramrazi, D. Haberer, G. de Oteyza Dimas, F. R. Fischer, S. G. Louie and M. F. Crommie, *Nat. Nanotechnol.*, 2015, **10**, 156-160.

148. L. Brey and H. A. Fertig, *Phys. Rev. B*, 2006, **73**, 235411.

149. M. Ezawa, *Phys. Rev. B*, 2006, **73**, 045432.

150. J. Liu, B.-W. Li, Y.-Z. Tan, A. Giannakopoulos, C. Sanchez-Sanchez, D. Beljonne, P. Ruffieux, R. Fasel, X. Feng and K. Müllen, *J. Am. Chem. Soc.*, 2015, **137**, 6097-6103.